ABSTRACT

Title of Thesis: **NOVEL ENDOSCOPE FOR SURGICAL GUIDANCE AND FUNCTIONAL BRAIN IMAGING**

Qinggong Tang, Master of Science, 2017

Thesis Directed By: Associate Professor, Yu Chen,
Fischell Department of Bioengineering

Optical imaging methods have become very powerful tools in biomedical research since they can achieve both high spatial and temporal resolutions. However, due to the effects of light scattering, the penetration depth of optical imaging methods is usually limited. Gradient refractive index (GRIN) lens that are 350–2,000 μm in diameter and provide micron-scale resolution have been shown to enable minimally invasive *in vivo* imaging of deep tissues. Based on GRIN lens, we developed a small hand-held optical coherence tomography (OCT) forward-imaging needle device for real-time epidural anesthesia surgery guidance and demonstrated its feasibility through *ex vivo* and *in vivo* animal experiments. Besides, to access subcortical brain structures, we combined voltage-sensitive dye imaging (VSDi) with GRIN lens to image neural activities evoked in thalamic barreloids by deflection of whiskers *in vivo* in the whisker system of rodents.

NOVEL ENDOSCOPE FOR SURGICAL GUIDANCE AND FUNCTIONAL BRAIN IMAGING

by

Qinggong Tang

Thesis submitted to the Faculty of the Graduate School of the
University of Maryland, College Park, in partial fulfillment
of the requirements for the degree of
Master of Science
2017

Advisory Committee:
Associate Professor Yu Chen, Chair
Assistant Professor Giuliano Scarcelli
Professor Yang Tao

Acknowledgements

First, I would like to thank Dr. Yu Chen, who gave me the opportunity to come to USA, and join this wonderful lab. During my time in UMD, Dr. Chen has taught me about the way to research, and the most important thing I have learned from him is how to act as a gentleman. We always discuss projects and progress like peers, and he never commands but suggests, which gave me more confidence to try more and move further.

I would like to thank the outstanding collaborators who have helped me along the way in my research. When I just got started in the lab, I had very little experience in animal experiments. Drs. Anthony Sandler and Kyle Wu from the Children's National Medical Center gave me a lot of encouragement, and explained the medical background to me with patience. I would also like to thank them for providing a great environment for preclinical studies on large animals. I would like to thank Dr. Reha S. Erzurumlu and Dr. Vassiliy Tsytsarev from University of Maryland School of Medicine. Dr. Erzurumlu is a very wise professor. He helped me go through my slides page by page and explained all the biological background with great patience, despite being really busy. I have already worked with Dr. Tsytsarev for more than four years. He always has a lot of novel ideas and has introduced me to many other great researchers.

I also want to acknowledge my great lab-mates, Dr. Hengchang Guo, Dr. Jianting Wang, Dr. Hsing-wen Wang, Dr. Chao-Wei Chen and Dr. Chia-pin Liang, for their companionship and mentorship.

Finally thanks to my family and girlfriend, your unconditional support and love always motivate me to move forward. Without you, I would not be so faithful and none of these would have been possible.

Table of Contents

List of Figures

Chapter 1: Introduction*

1.1 Motivation

1.1.1 Epidural anesthesia

Epidural anesthesia is one of the most widely used anesthesia methods [1]. It is usually given to a patient in need of post-operative pain control, painless labor, or chronic pain relief. The epidural space is only 2-7 millimeters in width and is located several centimeters deep from the back skin [2]. In general, the epidural needle needs to penetrate several tissue layers such as fat, supraspinous ligaments, interspinous ligaments, and ligamentum flavum before reaching the epidural space (between ligmentum flavum and dura). Therefore, accurate identification of the epidural space is critical for safe and effective epidural anesthesia or treatment of acute lumbar radicular pain with epidural steroid injections [3]. Due to lack of visual feedback to guide needle navigation, failure rate of epidural anesthesia is up to 20% [4], and the complication rate of peripheral nerve block approaches 10%, with the potential for permanent nerve damage [5]. In current clinical practice, the anesthesiologist's experience is what is mainly relied on[6]. Unfortunately, even for a skillful anesthesiologist, there is still around 5-10% of miss rate when performing "blind" punctures [7].

* Part of the contents in this chapter is modified and reproduced from "Tang, Q., Liang, C.-P., Wu, K., Sandler, A. & Chen, Y. Real-time epidural anesthesia guidance using optical coherence tomography needle probe. *Quantitative Imaging in Medicine and Surgery* **5**, 118-124 (2014)." and "Tang, Q. et al. In Vivo Voltage-Sensitive Dye Imaging of Subcortical Brain Function. *Sci Rep* **5**, 17325 (2015)." with permission.

Complications associated with epidural injections have been well documented [1]. In case of the dura mater puncture, a complication caused by cerebrospinal fluid leakage occurs, rendering the sufferer afflicted with post-dural-puncture headache (PDPH). Intravascular injection can result in cardiorespiratory arrest, central nervous system toxicity, and ischemic neurologic events in the spinal cord and brain [1, 8]. Spinal cord damage and paralysis after injection within the spinal cord have also been reported [9, 10]. Therefore, it is important that one can be guided by an objective tool that is capable of significantly improving the success rate during the epidural procedure [11].

1.1.2 Brain functional imaging

Neurons are the most essential units of the nervous system. To understand how the brain perceives the external world, it is desirable to observe neuronal functions in the brain during perception [12]. Localization of neural activities in different levels of brain, or in other words, functional brain mapping, has been one of the fundamental tasks for many generations of neuroscientists within the last hundred years [13] . Understanding functional wiring of neural circuits and their patterns of activation following sensory stimulations is a fundamental issue in developmental neurobiology. Furthermore, charting the activity patterns of these neural circuits will undoubtedly reveal cellular and molecular mechanisms of the wiring of the brain and serve as a tool with which one can learn more about brain disease processes and the effects of treatments. All of these can be utilized in their own right to aid in the development of drugs and treatment [14], such as Parkinson's disease and Alzheimer's disease.

Neuronal circuits are organized at diverse spatial scales, from subcellular compartments such as dendrites to local neuronal populations to whole brain areas.

For understanding how information is encoded in neuronal circuits, it is essential to record activity from a large number of neurons in different depth scale in living animals[15].

Optical methods have been proven to be a very useful technique in monitoring neural responses in the central nervous system, as they offer advantages for studying functional organization [16]. There are significant benefits for using light to image living tissue. Most importantly, light can provide exquisite sensitivity to functional changes, either via intrinsic changes in absorption, fluorescence, or scattering, or through the use of extrinsic contrast. Oxy- and deoxyhemoglobin (HbO_2 and HbR) are the most widely measured intrinsic chromophores, alongside cytochromes and metabolites, which have distinctive absorption or fluorescence characteristics[14]. Absorbing and fluorescent dyes, as well as cutting-edge transgenic methods, can also provide highly specific optical contrast enhancement, often capable of actively reporting functional parameters such as changes in membrane potential or ion concentrations[17]. However, most optical methods only offer surface information and do not provide depth resolution of functional responses[18]. The major challenge of optical imaging is to overcome the effects of light scattering, which limits the penetration depth and achievable imaging resolution[19].

1.2 Background

1.2.1 Optical coherence tomography (OCT)

Optical Coherence Tomography (OCT) is a non-invasive technique for obtaining sub-surface images of translucent or opaque materials. OCT can be regarded as an

optical analog of ultrasound except that it utilizes near infrared light rather than sound [20-24]. The technique is gaining traction within the medical community because it provides real-time imaging of tissue architecture at near-microscopic resolution. Furthermore, OCT does not utilize ionizing radiation, and no special preparation of the patient is required prior to imaging. There are mainly two types of OCT: time domain OCT (TD-OCT) and Fourier-domain OCT (FD-OCT), with FD-OCT having better sensitivity and faster imaging speed [25-27]. Apart from imaging the difference in tissue scattering properties, it is also feasible to utilize for more contrast mechanisms. There are three main extensions of OCT for functional imaging of tissue physiology: Doppler OCT [28-30], speckle variance OCT [31] [32] [33], and polarization-sensitive OCT (PS-OCT) [34] [35] [36] , which can provide supplementary information in addition to intensity variation.

Raphael et al. demonstrated the feasibility of OCT to resolve structures such as arteries, nerves and dural punctures in *ex vivo* animal studies [37]. Using micro-optics, OCT can be miniaturized into needle imaging devices to perform minimally invasive procedures [38-40]. Our group has developed a small-diameter (0.5 mm) forward-imaging OCT needle that can provide high-resolution structural images together with high-contrast Doppler flow images in real time [40]. We demonstrated that the probe can visualize artery, vein, and nerve structures in front of the needle in animal models *in vivo* [11].

1.2.2 Gradient refractive index (GRIN) lens

In order to access to deeper brain structures, we propose to apply the GRIN micro-lens, which is 350 –2,000 μm in diameter and provides micron-scale resolution [41]. These GRIN lenses are designed as needle type probes to enable minimally invasive *in vivo* imaging of individual cells in deep tissues [41, 42].Unlike conventional lenses that refract light at curved surfaces, GRIN lens are not ground to shape and can be cheaply fabricated in sub-millimeter sizes (e.g., 100 –2,000μm) suitable for insertion into solid tissue[43, 44].

GRIN lenses exhibit a spatially varying refractive index, because the glass is inhomogeneously doped with a cation species, such that cation density is typically highest at the central axis of the lens and declines toward the periphery [43, 45]. This leads to a refractive index profile that declines approximately quadratically with radial distance from the central axis of the lens (Fig. 1) [44 45]. In a ray description, total internal reflection occurs in a gradual manner as light passes from central regions to peripheral regions of lower index, causing light rays to travel down the cylindrical lens axis in an approximately sinusoidal path[45]. The axial length for one full sinusoidal cycle is called the pitch length.

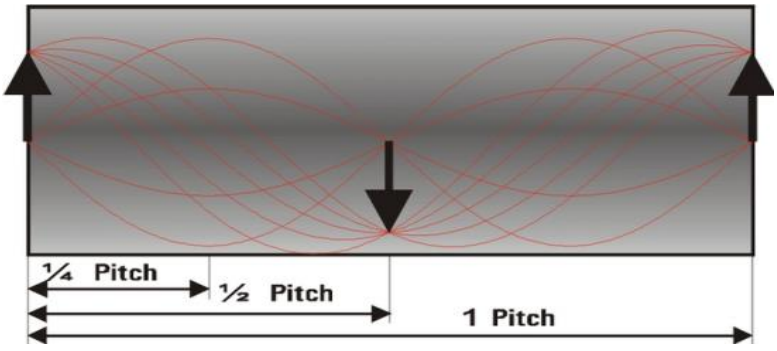

Figure 1. Ray traces within a GRIN focusing lens of different pitch length (From GRINTECH)

1.2.3 The whisker/barrel system in mice

The whisker/barrel system in mice is an excellent model to investigate the development, organization, function and plasticity of mammalian sensory systems[46]. Fig. 2 shows schematic of the whisker-to-barrel pathway. Sensory information from the whisker pad on the mouse snout is conveyed to the cerebral cortex via the trigeminal nerve to the trigeminal nucleus, then to the ventrobasal thalamus and to the barrel field in layer IV of somatosensory cortex. At all three levels of the trigeminal pathway (the brainstem, thalamus and cortex), presynaptic afferent terminals replicate the patterned distribution of whiskers on the snout. These presynaptic patterns are recognized by postsynaptic cells, which in turn form rings or neural modules around afferent patterns. These cellular patterns are called "barrelettes" in the brain stem, "barreloids" in the thalamus and "barrels" in the cortex [47]. Stimulation of a single whisker evokes neural activity in its corresponding barrel, barreloid, and barrelette [48]. Because of their ease of access, identification and close to surface location, the barrel fields have been the subject of numerous imaging studies with a variety of approaches [48-52]. In contrast to imaging of the neocortex, functional mapping of the subcortical structures using optical methods was technically challenging and limited [48, 53].

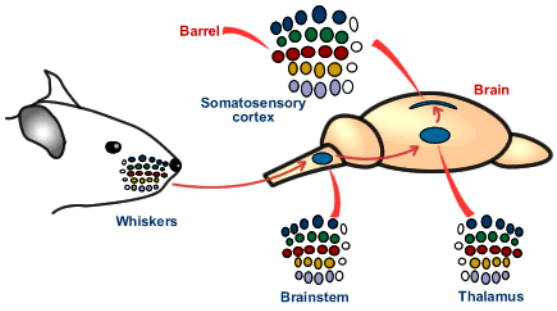

Figure 2. Schematic of the whisker-to-barrel pathway [54].

1.2.4 High-speed CCD camera based VSDi

Voltage-sensitive dye imaging (VSDi) appears to be one of the best tools in understanding how the large networks of neurons work (Fig. 3). VSD imaging offers an opportunity to study the activity of neuronal ensembles *in vivo* with relatively high spatial resolution (up to 20μm) and high temporal resolution (up to tens of microseconds) which is comparable with electrophysiology [55]. VSDs are chemical compounds that change optical properties in response to a change in membrane's electric field intensity [56] . Dye molecules bind to the membrane and convert changes in membrane potential into the energy of the emitted photons, so changes in

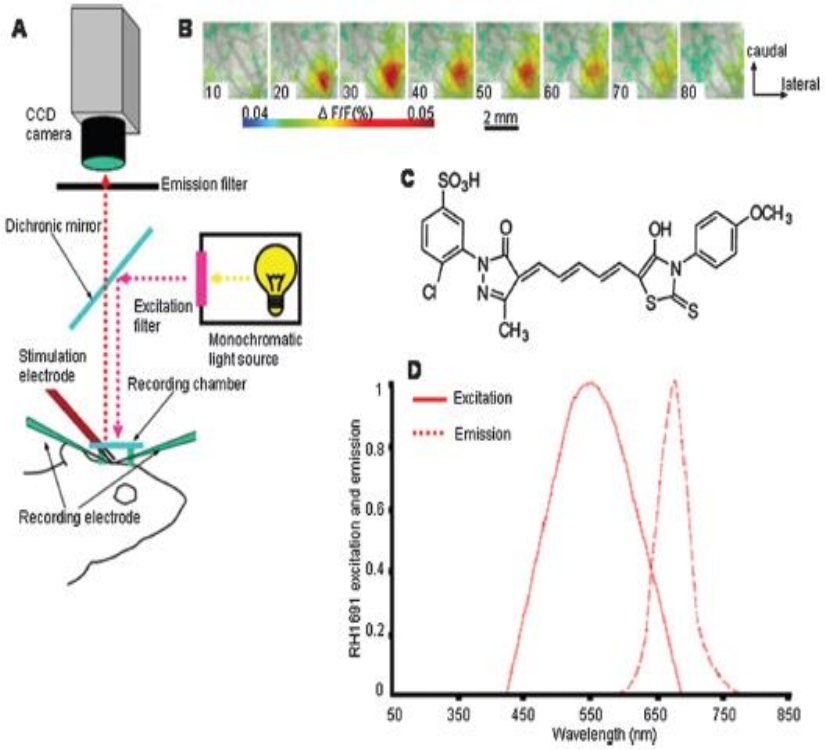

Figure 3. Voltage-sensitive dye optical imaging setup

(A) Main parts of the voltage-sensitive dye optical imaging setup. (B) Voltage-sensitive dye optical images of the somatosensory cortex showing single-whisker stimulation fluorescence changes, the time after stimulus onset (ms) is indicated at the bottom left corner of each image.(C) RH1691, one of the most common voltage-sensitive dye molecule. (D) Excitation and emission spectrum of the RH1691 voltage-sensitive dye [57, 58].

membrane potential will cause measurable changes in the fluorescence of the dye [59]. Since a large percentage of the total membrane area is dendritic, VSD signals reflect both spiking and synaptic activities [60]. During *in vivo* imaging, the sample is illuminated by excitation light of the VSD, and the fluorescent signal is recorded by a high-speed CCD camera through appropriate optical filters. The temporal resolution of the system is determined mainly by the parameters of the CCD camera [14]. However, since CCD cameras integrate the back-scattered light from various depths, this approach is only particularly useful for generating functional images of neural circuit dynamics in superficially located brain structures such as the cortex [61] [56]

1.3 Goals and objectives

The novel device we propose in Chapter 2 would allow real-time, *in-vivo* visualization of tissue structures during needle-based interventions without relying on external sources of ultrasound or ionizing radiation and the complexity of interpreting three dimensional planes. With the nerves, arteries, veins and other relevant tissue structures clearly differentiated and visualized at the needle tip, the proposed device will enhance clinical outcomes with regards to complication rates, induced pain, and procedure failure when compared to standard practice. Furthermore, this technology could be used independently of current ultrasound techniques or in combination with current practice techniques to enhance outcomes. Our ultimate goal is to create and develop a novel methodology of needle-based interventions to significantly enhance efficacy and reduce complications while minimizing pain and discomfort for patients.

GRIN lenses can relay current using th VSDi system from the cortical surface to deep brain. The research in Chapter 3 aims to develop and validate novel optical

imaging methods for neuronal functions research beyond the surface. The high speed, high resolution and minimally novel methods will be a major breakthrough in investigating responses of neuronal networks at various subcortical and deep regions following sensory stimulation, and will allow us to thoroughly study the neuron circuits *in vivo* at different levels.

Chapter 2: OCT needle probe for epidural anesthesia guidance*

2.1 Introduction

The most common method used in identifying epidural space is called "loss of resistance" (LOR) to either air or saline [62-64]. However, up to 10% of epidurals fail to provide adequate analgesia because of incorrect catheter placement using the LOR technique [65]. In more challenging procedures such as cervical epidural injections, the LOR technique can be inaccurate in up to 53% of cases when used without image guidance [66]. To address these difficulties, needle insertion under ultrasound guidance and fluoroscopy has been introduced [4, 65]. However, ultrasound guidance is challenging because of the complex and articulated encasement of bones that allows only a very narrow acoustic window for the ultrasound beam [4]. Fluoroscopy has no soft tissue contrast, and therefore cannot differentiate critical tissues such as blood vessels and nerves, which are important targets to locate/avoid during the insertion of needle [67]. Furthermore, due to low resolution, fluoroscopy-guided procedures are especially difficult for cervical and thoracic epidural anesthesia where the epidural space can be as narrow as 1-4 mm [11, 68].

To improve the accuracy of epidural space identification, Ting et al. developed an innovative optical-fiber-based technique for epidural needle placement

---

* The contents in this chapter is reproduced from "Tang, Q., Liang, C.-P., Wu, K., Sandler, A. & Chen, Y. Real-time epidural anesthesia guidance using optical coherence tomography needle probe. *Quantitative Imaging in Medicine and Surgery* **5**, 118-124 (2014)." with permission.

that uses 532 nm and 650 nm light reflection to discriminate the ligamentum flavum and dural tissues [67, 69, 70]. However, the amplitude of light reflection can be influenced by the direction of the needle bevel, thereby complicating the determination of threshold values [70]. Using this approach, approximately 80-85% in sensitivity and specificity has been reported [70, 71]. Rathmell et al. developed a novel epidural needle that acquires the entire optical reflectance spectra (500-1600 nm) from tissue close to the beveled surface [3, 72]. Using spectral unmixing algorithms, the accuracy of epidural space identification can be improved by quantification of blood versus lipid contents [3, 72]. Nevertheless, several confounding factors may decrease the accuracy of quantification, such as myoglobin in muscle and carotenes in epidural fat [3]. Furthermore, spectroscopic measurements can be influenced by the adjacent tissue layers, especially when the tissue geometric arrangement is altered by the pressure imparted by the needle [3, 11].

In this study, we investigate the feasibility of guiding epidural interventions using an emerging optical imaging technology named optical coherence tomography (OCT). Our group has developed a small-diameter (0.5 mm) forward-imaging OCT needle that can provide high-resolution structural images together with high-contrast Doppler flow images in real time [40]. We demonstrated that the probe can visualize artery, vein, and nerve structures in front of the needle in animal models *in vivo*. In the present study, we further miniaturized the handheld device and demonstrated the feasibility of OCT needle in identifying different tissue layers along the insertion to epidural space on *ex vivo* porcine spinal tissues and an *in vivo* swine model [11].

2.2 Experimental Setup

2.2.1 OCT Needle Imaging Device

The OCT needle imaging system is similar to the previous reported prototype (see Fig. 1a) [40]. This frequency-domain OCT system utilizes a wavelength-swept laser as light source which is centered at 1310 nm with 100nm bandwidth [11]. The wavelength-swept frequency is 16 kHz with 19 mW output power. A Mach-Zehnder interferometer (MZI) receives 3% of the laser output power and uses it to generate a frequency-clock signal with uniformly spaced optical frequency to trigger the sampling of the OCT signal into data acquisition board. The remaining 97% of the laser power is split evenly into the sample and reference arms of a fiber-based Michelson interferometer. The reflected signals from the sample and reference arms form interference fringes at the fiber couple (FC). The interference fringes from different depths received by a balanced detector (BD) are encoded with different frequencies. Depth-resolved tomography can be obtained by analyzing the frequency spectrum of the interference fringes through Fourier transform [11].

During imaging, the laser spot is scanned by a galvo scanning mirror (GSM) and delivered into tissues with special relay optics called gradient-index (GRIN) rod lens [73]. The GRIN rod lens design eliminates the need to scan optics in the constrictive distal end and thus significantly reduces the probe size. The axial resolution was optimized with careful dispersion matching at the reference arm using another GRIN-rod lens that had the same specifications as the one used in the sample arm. Both the lateral and axial resolutions in tissue are around 13 μm. The needle imaging device is equipped with a 0.5-mm-in-diameter GRIN rod lens, and the resulting lateral imaging

field-of-view (FOV) is around 0.44 mm [11]. The sensitivity of system was optimized to 92 dB, calculated using a mirror with a calibrated attenuator. The total outer diameter (O.D.) including the GRIN rod lens and the protective steel tubing is around 0.74 mm, which can be fitted into the clinically-used 18 gauge epidural needle. Fig. 1(b) shows the picture of the miniaturized hand-held needle device. The hand-held portion of this device measures around 13 cm (L) x 4 cm (W) x 4 cm (H), and it enables insertion of the needle device by hand during experiments [see the photo inset in Fig. 1(a)].

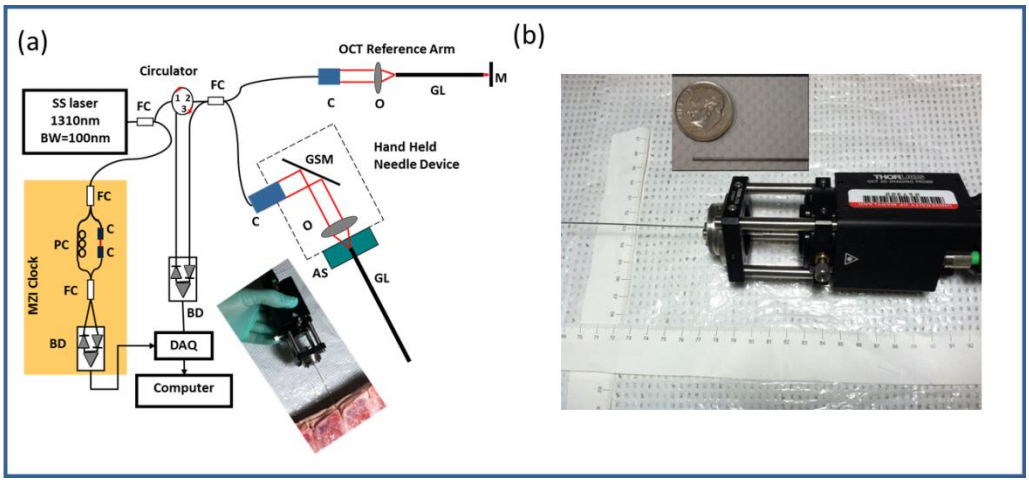

Figure 1. Hand-held OCT needle imaging system
(a) Schematic of the hand-held OCT needle imaging system. FC: fiber coupler; PC: polarization controller; C: collimator, BD: balanced detector, DAQ: data acquisition board, M: mirror, GSM: galvonometer scanning mirror, O: objective lens, AS: alignment stage. (b) Hand-held part. The inset image shows the GRIN needle placing aside of a US dime [11].

2.2.2 Animal Imaging Experiments

All of the procedures are approved by the Institutional Animal Care and Use Committees (IACUC) at both the University of Maryland and the Children's National Medical Center (CNMC). For *ex vivo* tissue imaging, 6 porcine spinal tissues were purchased from local slaughter house, and imaged freshly with several hours after tissue harvest. During imaging, the imaging needle was inserted manually into the

tissue. The insertion depth was measured for each recorded image to facilitate the localization of needle tip.

For *in vivo* experiments, 3 Yorkshire piglet (~8 kg) models were used. The piglets fasted overnight prior to the day of surgery. The animals were pre-medicated using Ketamine (20mg/kg) and Xylazine (2mg/kg) and weighed. They were then transported to the dedicated animal operating room at CNMC where they were intubated and ventilated, with general anesthesia maintained using Isoflurane. The piglet's neck was pinched with toothed forceps to ensure adequate anesthesia. The piglet's bilateral groin areas, neck, and lower back was clipped for preparation of procedures. The same areas were then aseptically prepared using Chlorhexidine scrub twice to maintain sterility of the procedure. Upon successful general anesthesia, OCT needle imaging was carried out under sterile condition. During imaging, the animals were monitored continuously using ECG monitoring and a pulse oximeter. Vital signs were continuously observed to ensure adequate anesthesia and animal well-being. After experiment, the animals were euthanized compulsorily. Beuthanasia (1ml per 4.5lb weight) was administered intravenously into an ear vein. Animal death was determined by listening for heart sounds and respiratory activity. Bilateral thoracotomy was performed as secondary terminal procedure.

Fig. 2 shows the experimental setup for *in vivo* animal experiments. In order to obtain a smooth insertion process with constant speed and avoid bulk motion due to hand operation, the hand-held part of the OCT needle device was mounted on a motor stage which was controlled by a motor controller (ESP301, 3 Axis Motion Controller, Newport Corporation). The motor stage was fixed on an articulated arm for easy

adjustment and stability. During the experiment, the skin of the insertion location was opened and the hand-held needle was slowly inserted into different depths inside the tissue. OCT images were acquired corresponding to different structures during the insertion from the supraspinous ligaments to the spinal cord.

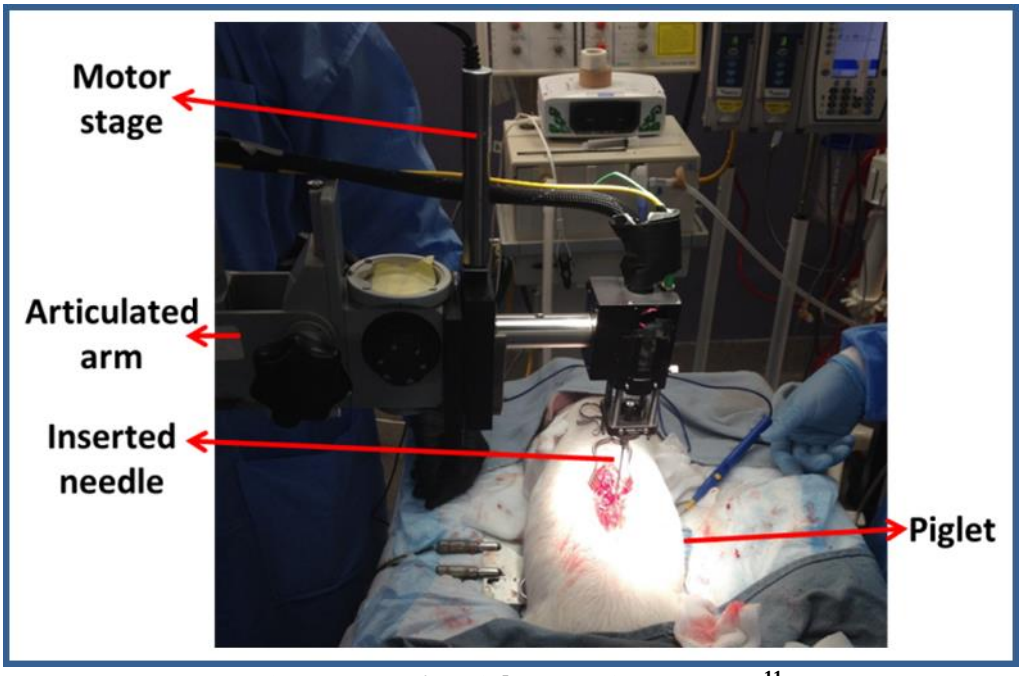

Figure 2. *In vivo* piglet experiment setup [11]

2.3 Results and Discussion

2.3.1 *Ex vivo* Porcine Tissue Experiment

The feasibility of our system for epidural anesthesia guidance was first investigated using an *ex vivo* porcine spine model. Fig. 3 shows representative results of the OCT-guided insertion. Fig. 3(a) shows the photo of the pig spine used for experiment. It was cut in sagittal view and the corresponding structures can be identified based on anatomy as shown in Fig 3(b).

During experiment, the hand-held needle was slowly inserted into different positions in the tissue. OCT images were acquired corresponding to different structures during the insertion from the skin to the epidural space. The OCT images shown in Fig. 3(c) clearly show different tissue types. The fat tissue is featured with pockets of adipocytes. The ligaments are featured with bright and dark stripes due to

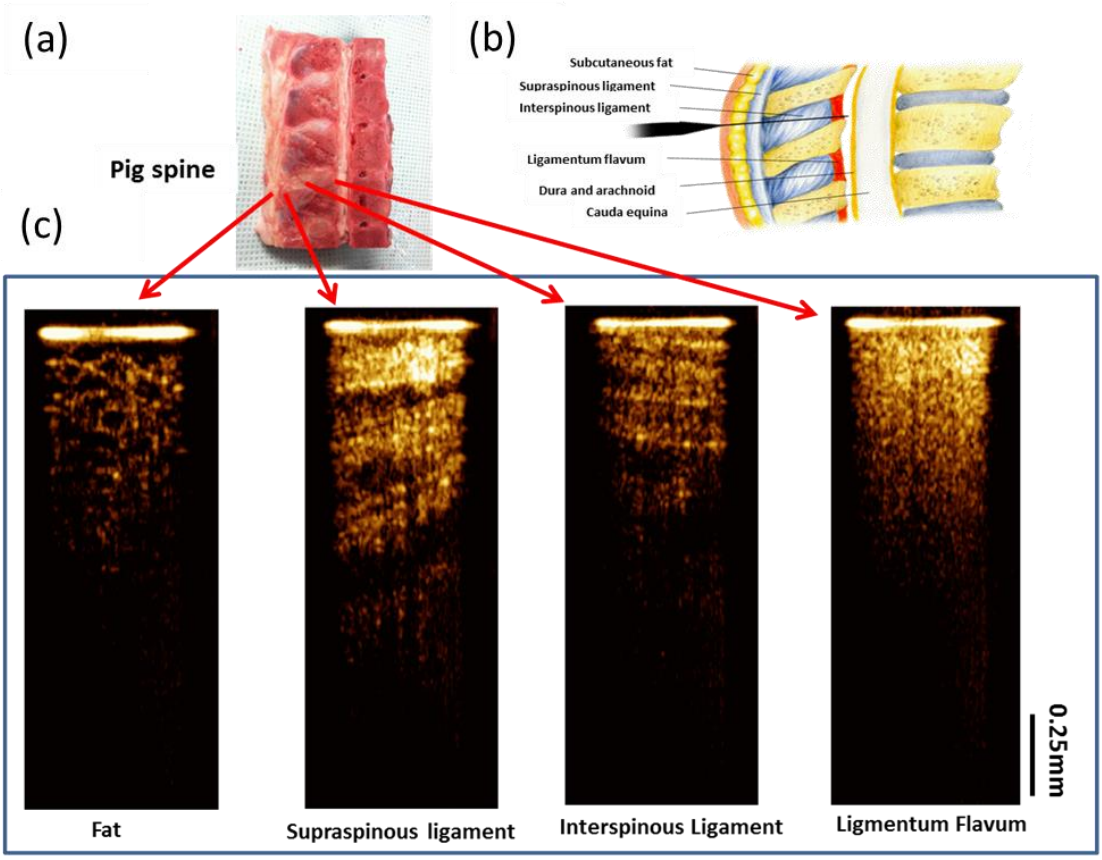

Figure 3. Needle OCT images of spinal tissues *ex vivo*
(a) The porcine spine tissue used for experiment. (b) Anatomy of lumbar spine (sagittal view). Image is adapted from http://pharma-munvar.blogspot.com/2010/02/local-anesthetics-local-anestheticsla.html. (c) Cross-sectional OCT images acquired by GRIN needle device corresponding to different tissues.

birefringence effects. The supraspinous and interspinous ligaments can be differentiated by their different fiber orientations and thickness of fiber bundles. For ligmentum flavum, its OCT image is bright (hyper-reflective) and homogenous.

These results indicate that it is feasible to distinguish epidural space and ligmentum flavum since the epidural space is filled with fat and blood vessels.

2.3.2 In vivo Piglet Experiment

Fig. 4 shows the OCT needle images acquired from different tissue types *in vivo*. Consistent with the *ex vivo* results, the supraspinous (Fig. 4B) and interspinous (Fig. 4C) ligaments can be differentiated by their different fiber orientations and thickness

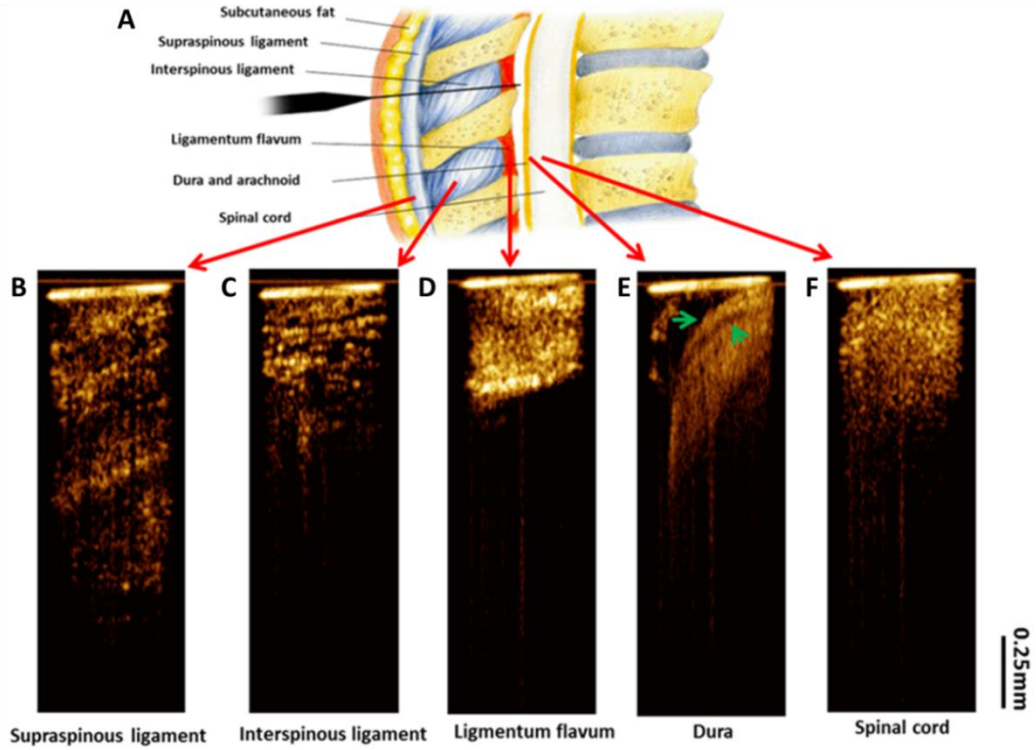

Figure 4. *In vivo* needle OCT-guided insertion
(A) Tissue layers through epidural needle insertion track. Image is adapted from http://pharma-munvar.blogspot.com/2010/02/local-anesthetics-local-anestheticsla.html. (B-F) *In vivo* needle OCT images corresponding to different tissues types: supraspinous (B) and interspinous (C) ligaments, ligmentum flavum (D), epidural space (E) with the dura membrane indicated by two green arrows, and spinal cord (F). The bright horizontal line at the top of each OCT image indicates the tip of needle.

of fiber bundles. Furthermore, penetration is much deeper in supraspinous ligaments. The OCT image of ligmentum flavum (Fig. 4D) shows bright and homogeneous reflectance. After ligmentum flavum, the probe reached the epidural space (Fig. 4E). The dura membrane, a very important landmark for epidural injection, can be identified. The anesthetist can stop the needle here and deliver drugs. Continuing the needle advancement, the needle probe penetrated the dura and reached the spinal cord (Fig. 4F). The OCT image of spinal cord shows prominent speckle patterns with the brightness between the dura and ligmentum flavum. These results demonstrate that there are characteristic differences between different structures, especially between ligmentum flavum and dura membrane or fat which is landmark for determine the positon of epidural space. The *in vivo* OCT images clearly show the feasibility of differentiating tissue types in real time, therefore, it will be beneficial to guide the anesthetists to identify the needle tip location during the epidural intervention.

2.4. Conclusion

We have developed an OCT forward-imaging needle device which can be integrated with an 18-gauge epidural needle and acquires OCT images in real-time for epidural anesthesia surgery guidance. The ability to identify tissues at different locations along the insertion to epidural space was demonstrated both *ex vivo* and *in vivo*. More *in vivo* experiments on animal models are necessary to further assess this device's potential to improve the rate of successful epidural anesthesia. In addition, we are in the process of developing quantitative imaging parameters such as tissue attenuation and texture for better classification of tissue types. With relevant tissue structures clearly visualized and differentiated at the needle tip, the OCT needle

imaging device is promising to enhance clinical outcomes with regards to complication rates, induced pain, and procedure failure when compared to standard practice. Furthermore, this technology could be used in combination with ultrasound/fluoroscopy to enhance outcomes.

Chapter 3: GRIN lens-based VSDi for deep brain functional imaging*

3.1 Introduction

Localizing and real-time monitoring of neural activities evoked by peripheral stimulation are important steps in understanding the functional characteristics of neuronal circuits in the brain [74]. Imaging plays an important role in associating the activities of single neuron and cell ensembles with physiological and anatomical properties of the organism. Various optical imaging methods using either reflectance or fluorescence photons have shown to be very promising in functional brain mapping [75]. Intrinsic Optical Signal (IOS) imaging[76, 77], Diffuse Optical Imaging (DOI) [78-80], Optical Coherence Tomography (OCT) [61, 81-84], Photoacoustic Tomography (PAT) [85], as well as Multiphoton Microscopy (MPM) [86, 87], provide neuroscientists an opportunity to observe, noninvasively, the anatomy of the living brain, and to monitor its functions *in vivo*[48] .

VSDi imaging offers an excellent opportunity to monitor the neural activity with high spatial and temporal resolution[88-91]. This method is based on the voltage-sensitive fluorescence probes, i.e., chemicals that change their optical features in response to the changes of the transmembrane electric field. In the experiment, the dye molecules bind to the neuronal membrane and convert changes in the transmembrane voltage into changes in fluorescence [75]. These changes are recorded by the optical imaging system and can be used for functional brain mapping[48].

---

* The contents in this chapter is reproduced from "Tang, Q. et al. In Vivo Voltage-Sensitive Dye Imaging of Subcortical Brain Function. *Sci Rep* **5**, 17325 (2015)." with permission.

Topographic neural maps of the sensory periphery have been known for a very long time. However, *in vivo* functional imaging of these maps is relatively new. The rodent whisker-barrel system is an excellent model to investigate the development, organization, function, and plasticity of mammalian sensory pathways. In this system neuronal modules, representing single whiskers on the snout, form at the brainstem (barrelettes), thalamic (barreloids), and neocortical (barrels) levels [92, 93]. Because of their ease of access, identification and close to surface location, the barrel fields have been the subject of numerous imaging studies with a variety of approaches [49-52]. In contrast to imaging of the neocortex, functional mapping of the subcortical structures using optical methods was technically challenging and limited [53]. Currently, miniature endoscopic probes offer a solution for deep brain imaging by overcoming the limited depth of intravital microscopy [94]. Taking advantage of this, we built a functional imaging system, which combines VSDi with a 1mm-GRIN rod lens to monitor temporal and spatial dynamics of neural activities in the thalamus following whisker stimulation. We imaged neural activity in the ventral posteromedial (VPM) nucleus of the mouse thalamus responding to single whisker stimulation. With this approach, we were able to obtain a functional map of the thalamic barreloids.

3.2 Methods

The experimental procedures were all in accordance with the National Institute of Health guidelines for the care of experimental animals (National Institute of Health, Committee on Care and Use of Laboratory Animals, 1996) and all experimental protocols were approved by the Animal Use and Care Committee of the University of Maryland.

3.2.1 Animal Preparation

We imaged voltage-sensitive dye optical signals in eight adult mice (B6 male and female, 20 - 30 g body weight, age 5 - 10 weeks). All animals were anesthetized with urethane (1.15 g/kg) with body temperature maintained at 37^0C with a heating blanket. The animal's head was placed in a stereotaxic frame. For surgical preparation, the head was shaved, and a midline cutaneous incision was made. The skin over the skull was retracted, and a cranial hole, 1.5 mm in diameter, was made using a dental drill [74]. A 10 μL Hamilton syringe, outer needle diameter 0.3 mm, was used to inject 0.3 - 0.5 μL voltage-sensitive dye RH-1691 (Optical Imaging Ltd, 1.0 mg/mL in the artificial cerebrospinal fluid (ACSF)) into the VPM using stereotaxic coordinates (-1.7 posterior, 1.6 lateral and 3.1 mm below dura mater)[95] in 5 minutes. The cranial opening was covered by a drop of high viscosity silicone oil to prevent drying and decrease brain pulsation [96]. Imaging was started 15-20 minutes after dye loading.

3.2.2 Experimental Setup

Fig. 1 illustrates the schematic of the needle-based VSDi imaging system. The system is equipped with a 1-mm diameter GRIN rod lens (NA 0.113; Go Foton Corporation), which provides an imaging field-of-view (FOV) of ~0.9 mm and relays the image from the mouse brain at the distal end of the needle probe back to the focal plane of the objective (Leica Objective Planapo 2.0x, M-series). The system utilizes a 637 nm laser diode as its light source, which is coupled with a single-mode fiber to shape its light beam. A diffuser is used to make the light more uniform. The light is collimated by an objective and goes through a dichroic mirror (650 nm, single edge

dichroic beam splitter; FF650-DiO1-50×70 mm; Andover Corporation). A shutter is applied to control the excitation light state and avoid dye photobleaching. The light is then coupled to the GRIN rod lens by the microscope objective. A custom-built motorized 3D micro-stage facilitates accurate light coupling between the objective and GRIN rod lens. The emitted fluorescent light is collected back through the GRIN rod lens, objective, dichroic mirror, an emission filter (695 nm, 695FG07-50,

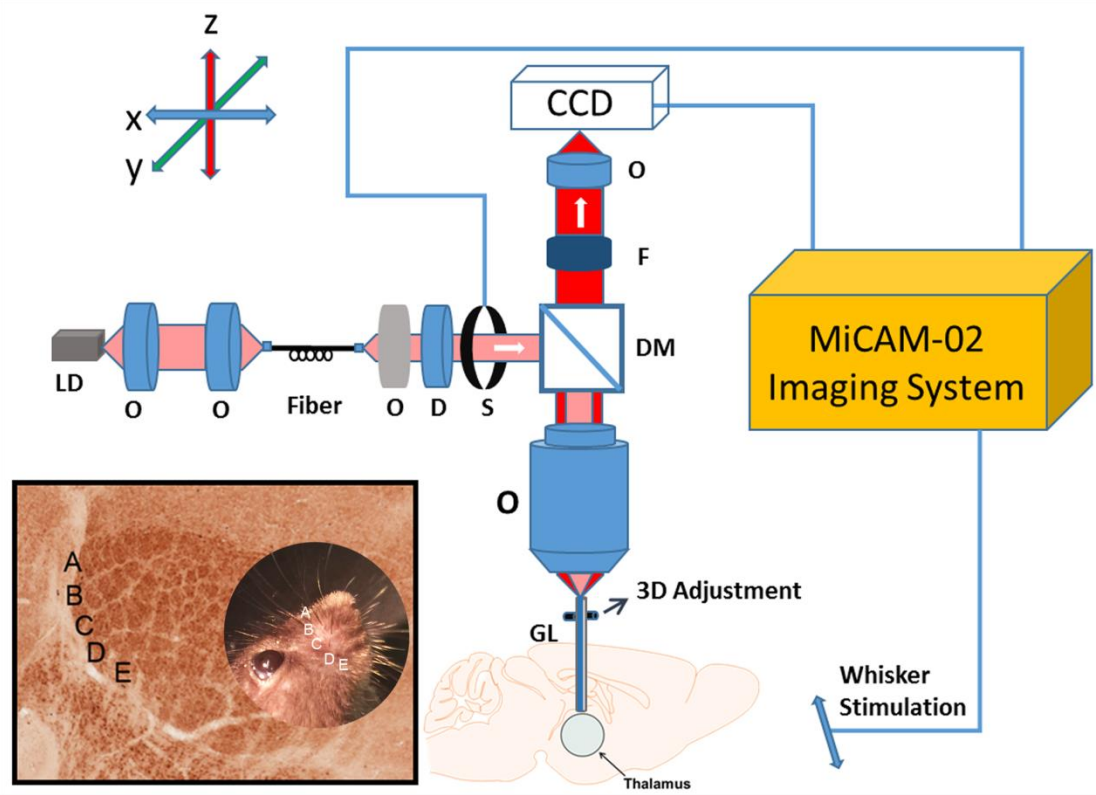

Figure 1. Schematic of the VSDi needle system

O: objective lens; S: shutter; D: diffuser; F: filter; DM: dichroic mirror; GL: GRIN rod lens. Bottom left inset shows barreloid organization with respect to the whisker pad (circled photo). Cytochrome oxidase stained section, dorsal is up, lateral is to the left. Whisker rows A-E are indicated.

Andover Corporation), and finally imaged on a high-speed CCD camera (MiCAM02-HR, SciMedia, Ltd). For deep tissue imaging, after aligning the GRIN rod lens to the objective, the GRIN-rod-lens probe was gently inserted into the anesthetized mouse

thalamus by moving up the animal stage slowly based on stereotaxic coordinates [48, 95].

3.2.3 Stimuli and Data Acquisition

Each experimental session consisted of 10 - 30 trials, with 200 frames per trial. Data acquisition rate was 5 ms/frame (200 Hz). For single stimulus experiments, the stimulus (whisker deflection) was presented at the 100th frame (one stimulus per trial). For dual stimulus experiment, the two stimuli were set at the 70th frame and the 120th frame, respectively. The pause between trials was 10 seconds. Fluorescence changes were calculated as $\Delta F/F$ (%) in the recording area using Brain Vision Analyzer (Brain Vision Inc., Tokyo, Japan). Before stimulation, all whiskers, with the exception of the designated whiskers used for experiment, were clipped close to the skin. To perform stimulation, a glass pipette (1.0 mm in diameter) fitted on an XYZ manipulator was aimed at the designated whisker. Air-puff stimulus (duration 10-20 ms) was applied through a Picospritzer pressure valve connected to the glass pipette [96]. The Picospritzer was coupled to the imaging system through the MiCAM-02 controller, so the air could be puffed onto the whiskers at precisely controlled time points. Trains of whisker stimuli were delivered and the associated changes in fluorescence signals were recorded in the contralateral thalamus. In addition, we also performed ipsilateral stimulation as control [93]. In some experiments muscimol (0.1 µl, 10 mM in ACSF), a selective $GABA_A$ receptor agonist, was injected at a depth of 300 µm below the cortical surface [97] .The injection was performed with a glass pipette (20 µm tip diameter) attached to a Nanojet II injector (Drummond Scientific, USA)[98]

3.2.4 Data analysis

For single stimulation experiments, the final ten pre-stimulus frames (i.e., 90-99th frame) were averaged as the baseline image. The baseline image was then subtracted from each subsequent frame to obtain changes in fluorescence signals. For dual stimuli experiments, the final ten pre-stimulus frames, i.e., 60-69th frame and 110-119th frame were averaged as the baseline for the 1st and 2nd stimulus, respectively. Pixels which exhibited a change in fluorescence ($\Delta F/F$) greater than 50% of the maximum change were identified as activated regions.[51]. Subsequently, we obtained pseudocolor maps of the areas activated by whisker stimulation. In the experiment exploring the effect of corticothalamic inputs, obtained data were expressed as mean ± standard deviation. Statistical analyses were then carried out using MATLAB. The student t-test was used to compare the signal amplitude and activated area (pixel number) in VPM before and after muscimol injection. $P<0.05$ was considered to indicate a statistically significant difference.

3.2.5 Histology

After the experiment, the animal was euthanized by barbiturate overdose and perfused by 4% paraformaldehyde and decapitated. The brain was extracted and sliced coronally (0.3 mm thickness) using a vibratome. The slice was photographed using fluorescence microscope. The probe track was superimposed.[95]

3.3 Results

3.3.1 Cortical signal recording

First we carried out an experiment to record the cortical signal corresponding to single whisker stimulation using our GRIN-rod-lens VSDi system. The purpose of this experiment was to confirm the performance of the needle-based imaging system. For imaging, the distal end of the GRIN rod lens was positioned above the recording

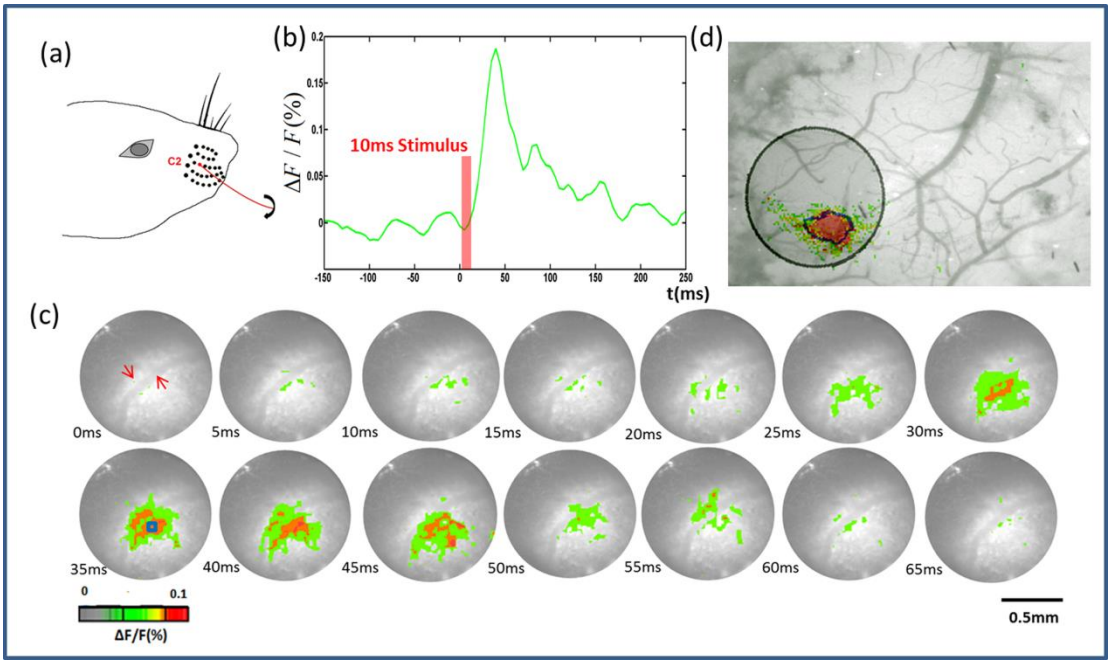

Figure 2. Cortical signal imaging

(a) C2 whisker stimulation. (b) Change in fluorescence (ΔF/F(%), ordinate) in response to stimulation. Fluorescence signal was calculated from the ROI (small blue square: 5 by 5 pixels) shown in Figure 2(c) at 35ms post-stimulation. (c) Voltage-sensitive dye optical images showing single-whisker (C2) stimulation fluorescence changes in the cortex. The stimulus onset was 0 ms. Time period after stimulation is indicated at the bottom left corner of each image. (d) The same area with the GRIN lens superimposed with image taken by conventional system. The black circle is the field view of GRIN lens and the black contour is the boundary of the activated area imaged by GRIN lens.

area and directed such that its optical axis was perpendicular to the cranial window. The focusing plane was set to 300 μm below the dural surface. As illustrated in Fig. 2(a), the C2 whisker was stimulated for a period of 10 ms. The signal appeared 20 ms after the stimulus onset, and reached its peak at about 40 ms after the stimulus onset. After reaching the maximum value, the activated signals decreased until returning to baseline [Fig. 2(b)]. The changes in activation area followed a pattern corresponding to the stimulation [Fig. 2(c)]. Blood vessels were visualized due to different light

absorption of the hemoglobin and the cortical tissue (labeled in red arrow in Fig. 2(c)). The results of cortical signal recording agreed well with the conventional VSDi system without GRIN rod lens, indicating that the GRIN-rod-lens imaging system is suitable for VSDi signal recording [51]. In addition, we imaged the cortex first with the conventional system and then the same area with the GRIN-rod-lens for comparison. As illustrated in Fig. 2(d), there was no notable difference in the boundary of the activity patterns.

3.3.2 Mapping VPM responses to stimulation of single whisker

Fig. 3(a) depictss C2 whisker stimulation. Fig. 3(b) shows changes in fluorescence (ΔF/F) in response to C2 whisker stimulation. Ipsilateral stimulation data was acquired as control. Fig. 3(c) shows the GRIN rod lens images of changes in fluorescence signals in response to contralateral C2 whisker stimulation. The signal appeared about 20 ms after the stimulus onset, and reached its peak at 55-60 ms after the stimulus onset. An interesting observation is that after reaching its maximum value, the activated areas started to spread at 65 ms after the stimulus onset (indicated by the red arrows in Fig. 3(c)). Another peak appeared at 95 ms, which may be due to the whisker swinging back after the 10-ms air puff stimulation. After 110 ms, the activated signals disappeared gradually.

3.3.3 Mapping VPM responses to stimulation of multiple whiskers

To further investigate whether the needle-imaging system could differentiate multiple whisker-evoked responses in the VPM, we performed a three-whisker stimulation experiment. C2, D2 and E2 whiskers were stimulated at the same time

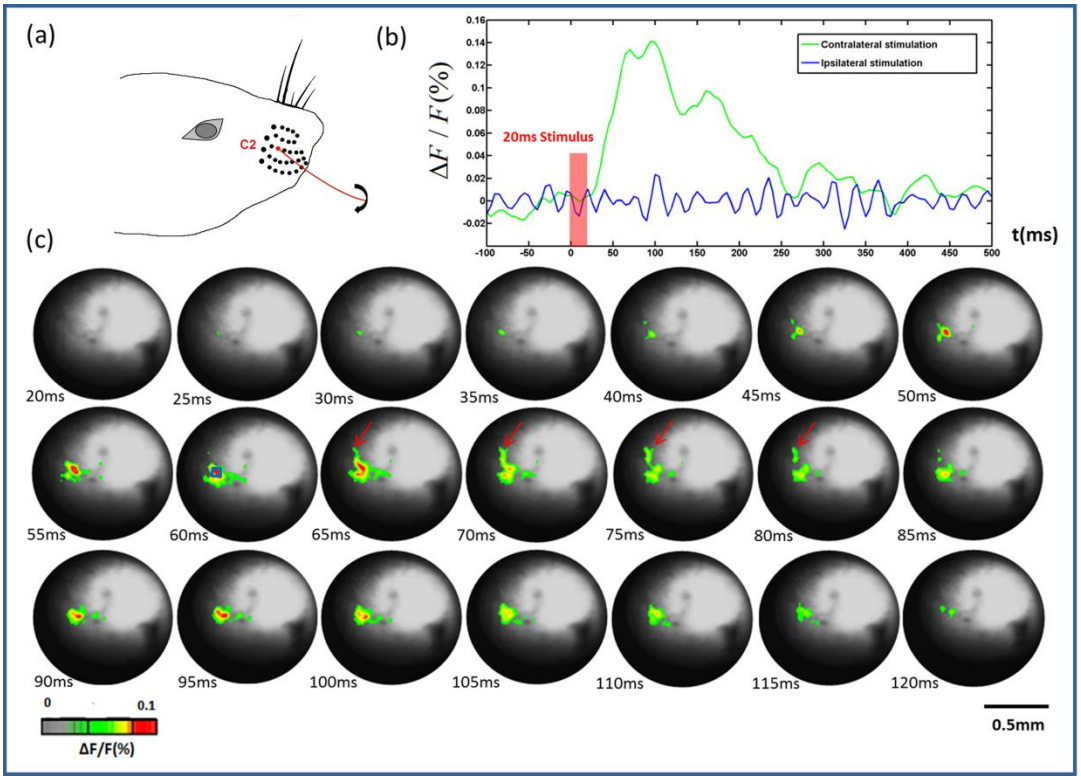

Figure 3. VPM responses to stimulation of single whisker

(a) C2 whisker for stimulation. (b) Changes in fluorescence (ΔF/F(%), ordinate) in response to C2 whisker stimulation. Fluorescence signal was recorded from the small blue square (5 by 5 pixels) marked on the image shown in Figure 3(c) at 60 ms. (c) Voltage-sensitive dye optical images showing single-whisker (C2) stimulation fluorescence changes in the thalamus. Time period after stimulation is indicated at the bottom left corner of each image.

[Fig. 4(a)]. Ipsilateral stimulation data was acquired as control [Fig. 4(b)]. Fig. 4(c) shows the signal appearance and diminishing in both activation area size and signal magnitude. At 50 ms, we can clearly see the three areas, which correspond to three different whiskers. In order to see the temporal response more closely, signals from the three "hot spots" areas[99-101] were plotted in Fig. 4(d). There was a clear 5 ms peak delay between one area and the other two that may be due to the different whiskers lengths. Fig. 5 shows the result of such an experiment in which whiskers B2 and E2 were stimulated at nearly the same time. B2 and E2 whiskers have a larger spatial

separation on the snout. In Fig. 5(c), we can clearly see two separate responses. There was also a clear peak delay of 10 ms between these two responses.

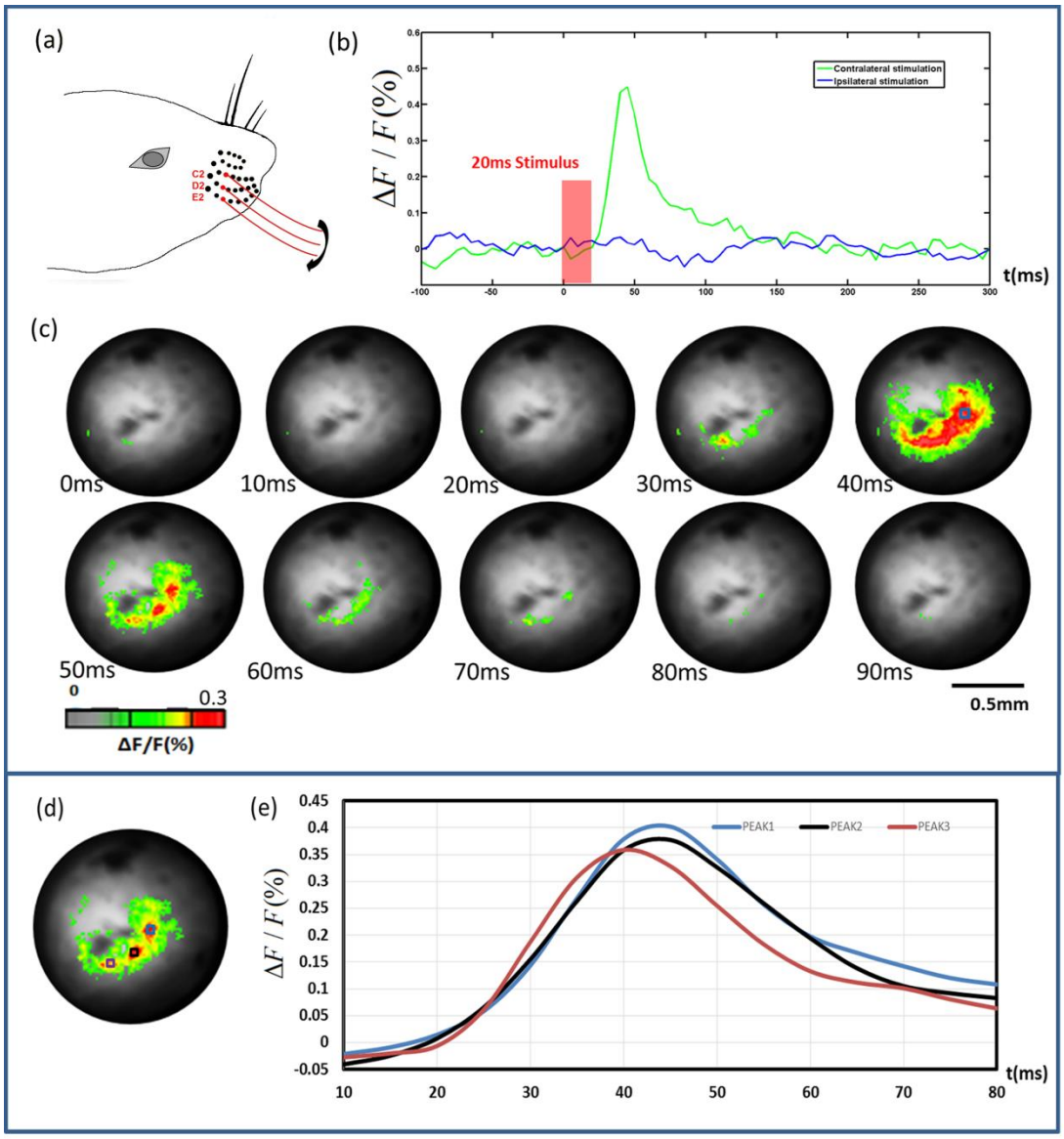

Figure 4. VPM responses to stimulation of multiple whiskers

(a) C2, D2 and E2 whiskers for stimulation; (b) Changes in fluorescence (ΔF/F(%), ordinate) in response to whiskers stimulation. Fluorescence signal was recorded in the small blue square (5 by 5 pixels) marked on the image shown in Figure 4(c) at 40 ms. (c) Voltage-sensitive dye optical images showing three whiskers stimulation fluorescence changes in thalamus. Time period after stimulation is indicated at the bottom left corner of each image. (d) Three areas chosen to plot the time course. (e) Changes in fluorescence (ΔF/F(%), ordinate) in response to whiskers stimulation. Fluorescence signal was recorded in the small squares marked on Figure 4(d).

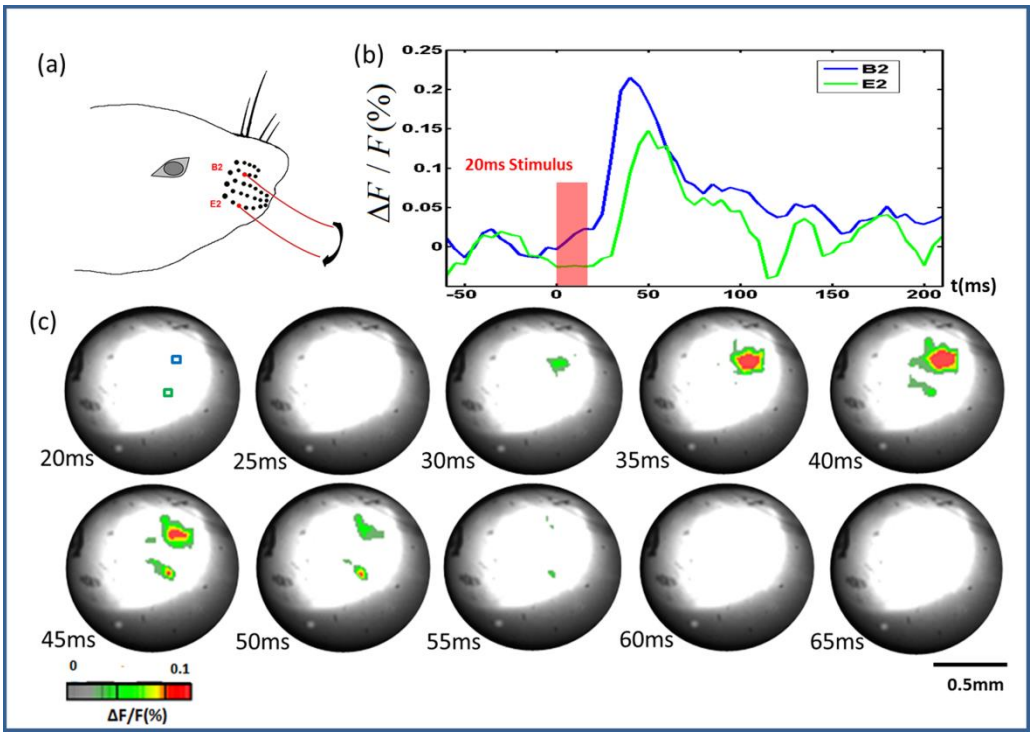

Figure 5. VPM responses to stimulation of B2 and E2 whiskers

(a) B2 and E2 whisker stimulation. (b) Changes in fluorescence (ΔF/F(%), ordinate) in response to whiskers stimulation. Fluorescence signal was recorded in the small blue and green squares (5 by 5 pixels) marked on the image shown in Figure 5(c) at 20ms. (c) Voltage-sensitive dye optical images showing two whisker stimulation fluorescence changes in the thalamus. Time period after stimulation is indicated at the bottom left corner of each image.

3.3.4 Mapping VPM responses to stimulation of multiple whiskers at different times

To further investigate whether the imaging system could differentiate the responses in the VPM when whiskers are stimulated at different times, we performed a time-difference stimulation experiment. B2 and D2 whiskers were used for stimulation [Fig. 6(a)]. Stimulation for B2 was set at 70th frame (350 ms) and stimulation for D2 was set at 120th frame (600 ms). The first response to B2 reached its maximum at 30 ms after B2 whisker stimulation, and the second response to D2 whisker reached its maximum at 35 ms after D2 whisker stimulation as shown in Fig.

6(b). The centers of the two response areas are separated by approximately 150 μm [Fig. 6(c)], which agreed well with the anatomy [102].

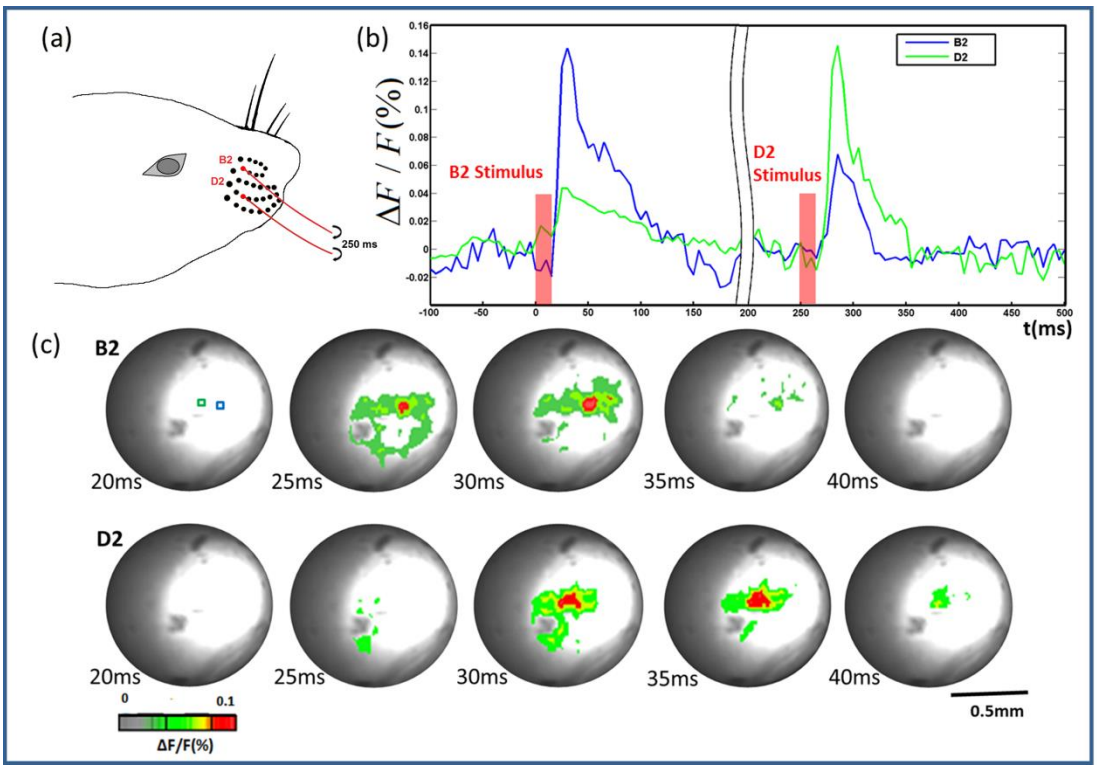

Figure 6. VPM responses to stimulation of B2 and E2 whiskers at different times
(a) B2 and D2 whisker stimulation; (b) Change in fluorescence (ΔF/F(%), ordinate) in response to whiskers stimulation. Fluorescence signal was recorded in the small blue and green squares (5 by 5 pixels) marked in Figure 6(c), B2, 20ms; (c) Voltage-sensitive dye optical images showing whisker (B2 and D2) stimulation fluorescence changes in the thalamus. Time period after stimulation is indicated at the bottom left corner of each image. The first row showing fluorescence response to B2 stimulation, the second row showing fluorescence response to D2 stimulation which was set 250 ms after B2 stimulation.

3.3.5 Exploring the effect of corticothalamic inputs to activities in thalamic barreloids

We performed imaging experiments in the thalamus of 4 mice following muscimol injection into the barrel cortex. Blocking cortical activity abolishes VSD signal in the cortex but not in the VPM. These are exciting new results that allow one to compare thalamic activation in the absence of corticothalamic inputs or when the cortex is silenced. Fig. 7(a) shows a wave plot of the changes in fluorescence

(ΔF/F(%), ordinate) in response to C2 whisker stimulation of the same area (5 by 5 pixels) in cortex before and after muscimol injection. We can clearly see that the responses in the cortex were inhibited by muscimol. In the following experiment, we first inserted the GRIN rod lens to the VPM based on the same procedure described above. Then the fluorescence signals in VPM before and after muscimol injection in response to contralateral C2 whisker stimulation were acquired as shown in Fig. 7(c). Compared to the signal without silencing the cortex, we observed that the activation area is much wider and scattered. Fig. 7(b) shows changes in fluorescence (ΔF/F(%), ordinate) in response to C2 whisker stimulation before and after muscimol injection. Fluorescence signal was recorded from the small blue and green squares marked on the images shown in Fig. 7(c) at 30 ms. We can see the signal magnitude is relatively low compared to the signal magnitude before muscimol injection. To quantify the effect of corticothalamic inputs to activities in the thalamic barreloids, the signal amplitude and activated area during stimulation were determined as shown in Fig. 8(a). The group with muscimol injection consisted of 3 data sets from 3 different animals. Control experiments (without muscimol injection) were performed on 4 data sets from 4 different animals. The signal amplitude in the group with muscimol injection was statistically smaller compared with the control group (P=0.0176). And activated area in the group with muscimol injection was nearly twice wide as the control group (P=0.0041). We conclude that our data may provide evidence indicating that feedback from the cortex plays a crucial role in shaping thalamic responses[103].

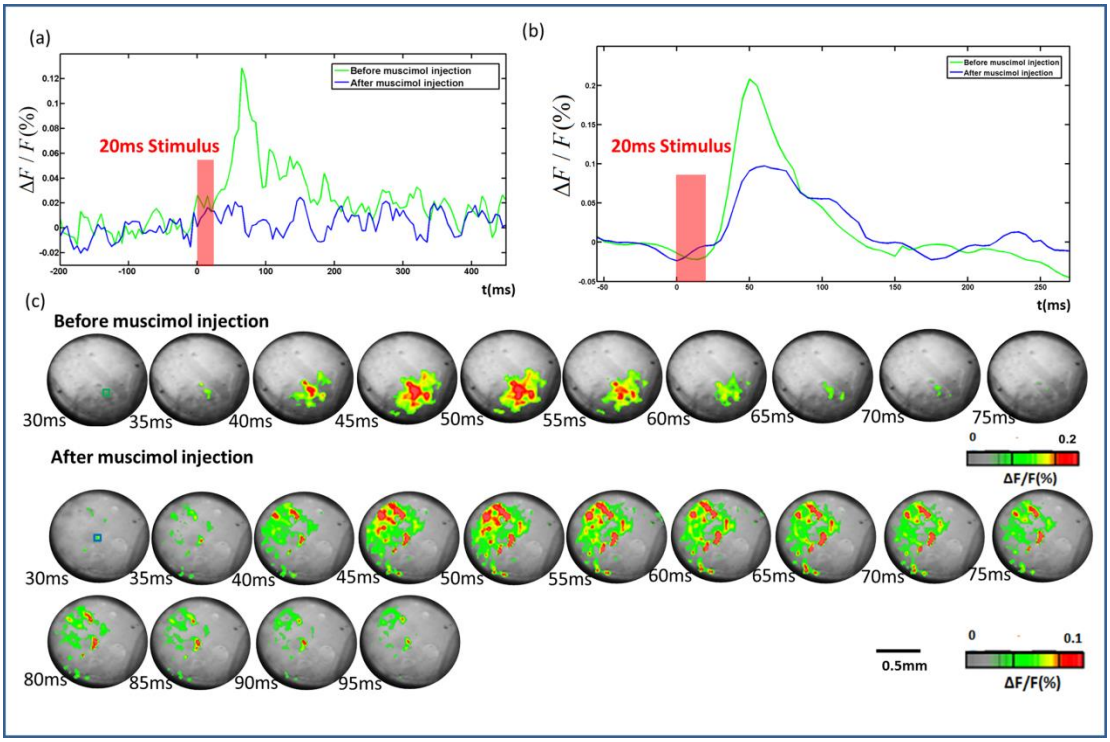

Figure 7. VPM responses before and after muscimol injection

(a) Changes in fluorescence (ΔF/F(%), ordinate) in response to C2 whisker stimulation of the same area (5 by 5 pixels) in cortex before and after muscimol injection. (b) Changes in fluorescence (ΔF/F(%), ordinate) in response to C2 whisker stimulation of the same area (5 by 5 pixels) in VPM before and after muscimol injection. Fluorescence signal was recorded from the small blue square marked on the image shown in Figure 7(c) at 30 ms. (c) Voltage-sensitive dye optical images showing single-whisker (C2) stimulation fluorescence changes in thalamus before and after muscimol injection. Time period after stimulation is indicated at the bottom left corner of each image. Different color maps were shown at the bottom of each images sequences.

Fig. 8(b) shows the GRIN rod lens track to the VPM in brain slice. Red color indicates RH-1691 dye fluorescence spread from the track of the GRIN probe. The positions of VPL, VPM and PO are labeled. While the GRIN rod lens causes a large area of damage to the brain, the barrel field of the somatosensory cortex and thalamocortical pathway are spared. This is mainly due to an angled approach to the VPM medially from the cortex and hippocampus. We can see the dye spread to VPM clearly and the GRIN rod lens is right above the VPM, which indicates that the stereotaxic coordinates we used allowed for precise location of the VPM.

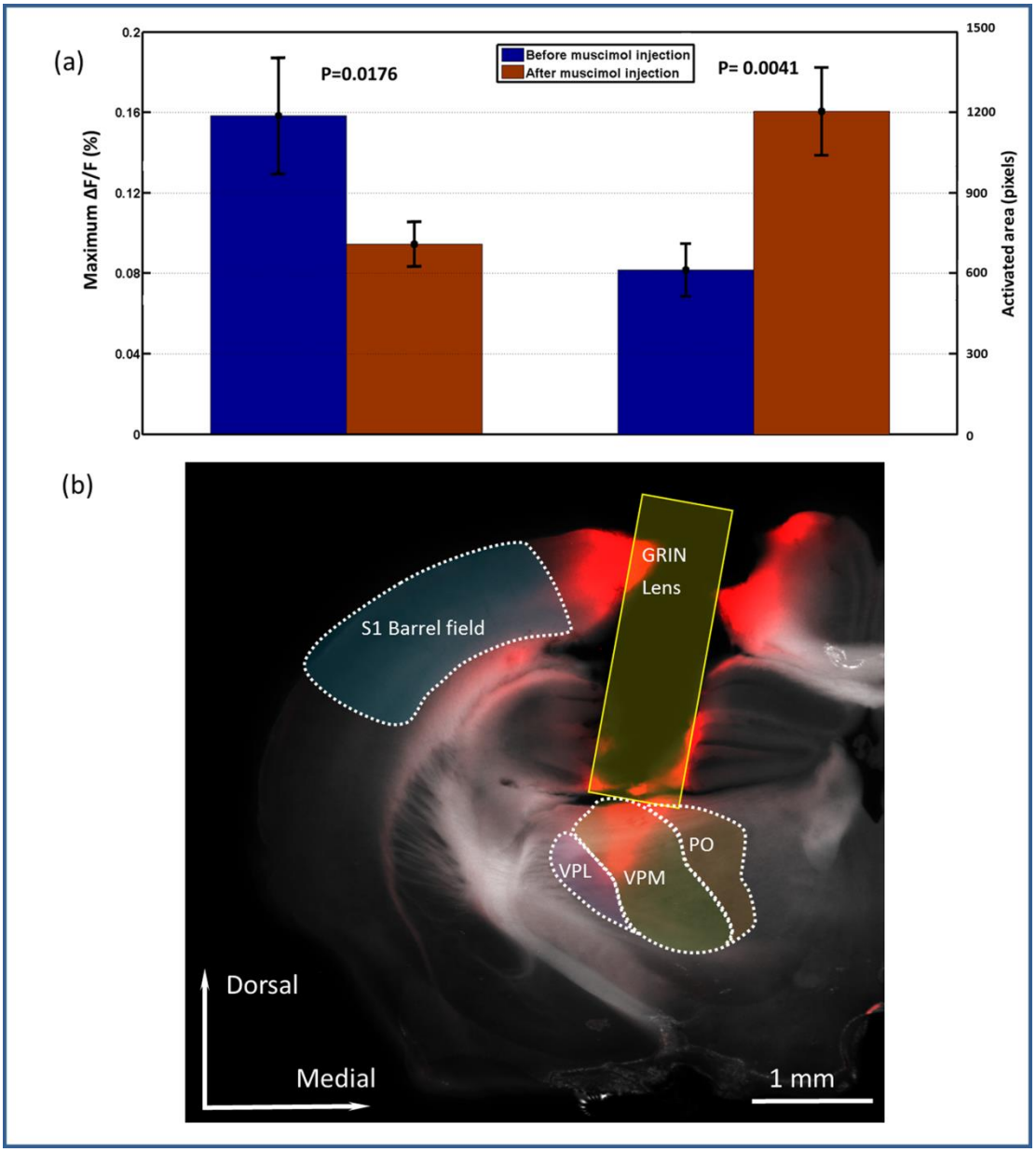

Figure 8. Statistics and histology

(a)Statistics of signal amplitudes and activated areas in VPM before and after muscimol injection. The signal amplitude of the group with muscimol injection (n=3, from 3 different animals) was statistically ($P<0.05$) smaller compared to control group (without muscimol injection: n=4, from 4 different animals). The activated area in the group with muscimol injection was statistically ($P<0.05$) larger than control group. (b) Brain slice taken 2.0 mm posterior from bregma and superimposed with the brain atlas [95](outlined and labeled areas). VPM - ventral posterior medial nucleus, PO - posteromedial thalamic nucleus, VPl - ventral posterolateral thalamic nucleus, S1- primary somatosensory cortex. Red color indicates RH-1691 dye fluorescence spread from the track of the GRIN probe and RH-1691 injection.

3.4 Discussion

Brain optical imaging has developed considerably within the last few decades [75]. Optical methods can offer both high spatial and temporal resolutions and are therefore particularly promising for measuring the hemodynamic, metabolic, and neuronal activity *in vivo* [61, 80, 85, 104, 105]. VSDi, which utilizes a high-speed CCD camera, offers an opportunity to study the activity of neuronal ensembles *in vivo* with relatively high spatial (up to 20 μm) and temporal resolution (up to few milliseconds, which is comparable to electrophysiology) [96, 106]. However, since CCD cameras integrate the back-scattered light from various depths, VSDi cannot detect depth-resolved functional activation[107]. In contrast with the single photon imaging, multi-photon microscopy has been used for functional neuronal imaging, and recent developments extend the penetration depths up to 1.6 mm in a mouse [104]. On the other hand, light penetration is fundamentally limited by scattering in the tissue. To overcome this limitation, several groups explored optical endoscopes. Miniature optical endoscopes are typically based on commercially available gradient-index (GRIN) rod lenses or imaging fiber bundles. GRIN rod lenses, which are typically 350–2,000 μm in diameter, can provide relatively high resolution, and have been used in deep brain imaging with relatively little injury [41, 42, 94, 108-111].

Many studies investigated information processing along the whisker-barrel system, using electrophysiological and morphological techniques. However, imaging studies in normal laboratory rodents and transgenic mice have been limited to the barrel cortex due to accessibility issues [51, 96, 112-115]. Light penetration and scattering limits the usage of the optical imaging methods in subcortical structures. Our present

in vivo results show that the combination of VSDi and GRIN optical probe can be utilized in imaging deep brain structures and can be adopted for use in freely moving animals through flexible imaging fiber bundle [116].

It is important to note the limitations of VSDi imaging at multiple levels of a sensory system. A notable one is the temporal resolution. The temporal resolution of the system we used is 5 ms, which is much longer than synaptic relays from the brainstem to cortex. Thus, we were not surprised that the latency of the VSDi signal, obtained from the VPM, and the time courses were similar for the optic signals recorded from the barrel cortex. In this regard, VSDi approach is not as sensitive as standard electrophysiological recording techniques because of the limited temporal resolution. The time differences between neural responses in the VPM and the barrel field can be just few milliseconds, which is shorter than our temporal resolution.

The VSDI signal and the physical relationship to barreloids in each experiment is not feasible at the moment. However if we express GFP or other fluorescent tags in barreloid neurons and activate them we might be able to pick up individual barreloids and specific activity patterns in relation to them. At the present time we can only compare the size of the activated areas in the VPM with respect to stained brain sections after imaging. Another limitation in imaging from deep brain structures is that the barreloids in the VPM are not all in the same plane from the tip of the GRIN-lens. The axes of the barreloids rows are not orthogonally located to the focal plane, and many of them are located slightly above or below the focus. Thus, the system we used does not have depth resolution for three-dimensional (3-D) neuronal maps. Lastly, the source of the fluorescence also has its own 3D structure located at an

undetermined distance from the focal plane is projected as 2D optical patterns. 3D imaging through GRIN-rod-lens needle microscope is also feasible using advanced image reconstruction algorithms[117]. Nonetheless, the compact size and functionality of GRIN optical devices in combination with VSDi are enabling imaging deep brain structures and functions in the mammalian brain *in vivo*.

Chapter 4: Conclusions and future directions

4.1 OCT needle probe for epidural anesthesia guidance

4.1.1 PS-OCT for epidural anesthesia

By collaborating with Dr. Sandler's group from Children's National Medical Center, we demonstrated the OCT needle probe for real-time epidural anesthesia guidance through ex vivo and in vivo animal experiments (Chapter 2). The major roadblock of the clinical translation of this OCT needle probe is that the sensitivity is not high enough and the contrast of different spinal structures are not very clear in the intensity imaging using a regular OCT only. Polarization-sensitive OCT (PSOCT), with six fold improvement of contrast [83], can potentially solve this problem by providing additional birefringence contrast. PS-OCT enables depth-resolved mapping of sample polarization information [118] , and is particularly useful when the nano-scale birefringence organization of tissues is difficult to differentiate using the intensity images from a regular OCT [119-121]. The PS-OCT system we built is based on the OCT system used in Chapter 2 [Fig. 1]. A polarizer is applied before the circulator to generate the linear polarized light. Several polarization controllers (PC) are also used in this system [121]. A polarization dependent balanced detector (PDBD, Thorlabs Inc., INT-POL-1300), which consists of two SMF based polarization beam splitters and two balanced photo-detectors, is utilized to collect the light in orthogonal polarization channels [121]. In Fig. 2, through PS-OCT microscope, the muscle and ligaments can be clearly differentiated from the thickness of the fiber. The fat is also easily separated form spinal cords since fat tissue has no birefringence contrast. Future work will be

integrating the PS-OCT with the needle device in Chapter 2 for providing supplementary guidance information during epidural anesthesia procedures.

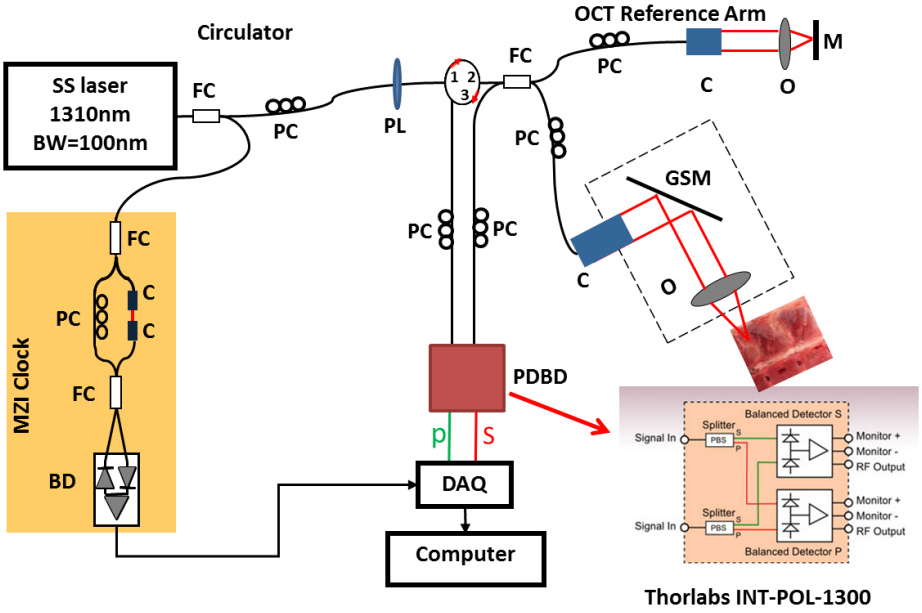

Figure 1. PS-OCT system

FC: fiber coupler; PC: polarization controller; C: collimator, MZI: Mach-Zehnder interferometer (frequency clocks), DAQ: data acquisition board, M: mirror, GSM: galvonometer scanning mirror, O: objective lens, AS: alignment stage, GL: GRIN lens needle, PL: polarizer, PC: polarization controller, PDBD: polarization dependent balanced detector.

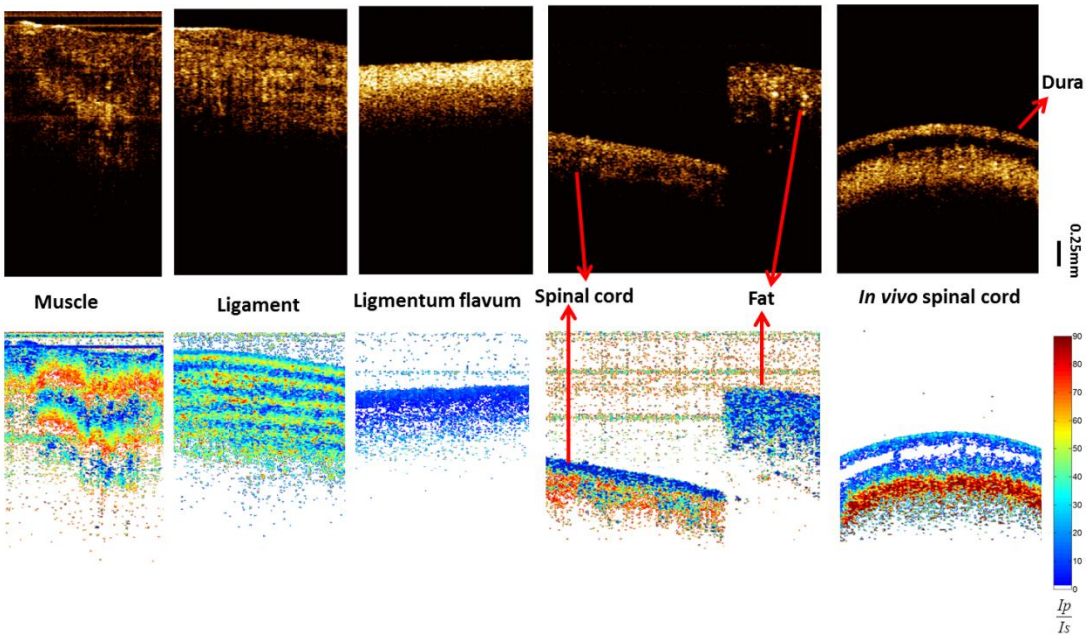

Figure 2. PS-OCT microscope data

4.1.2 System miniaturization

In Chapter 2, the hand-held portion of the OCT needle device has been miniaturized to around 13 cm (L) x 4 cm (W) x 4 cm (H), but the device needs to be further minimized and lightweight for integration with a stereotactic frame and to be easily operated by the surgeons. In the future work, the bulky scanning mirrors will be replaced by microelectromechanical (MEMS) mirrors (Mirrorcle) and the alignment stage will be replaced by a high precision ferrule (Vitrocom) [Fig. 3]. The small GRIN lens (GRINTECH) can also be used to replace the objective lens used in the current system [Fig. 3]. With these design changes, we can potentially build a needle-type, forward-imaging and hand-held OCT probe which can provide us with sample intensity signal, Doppler information and also polarization contrast in real time [Fig. 3].

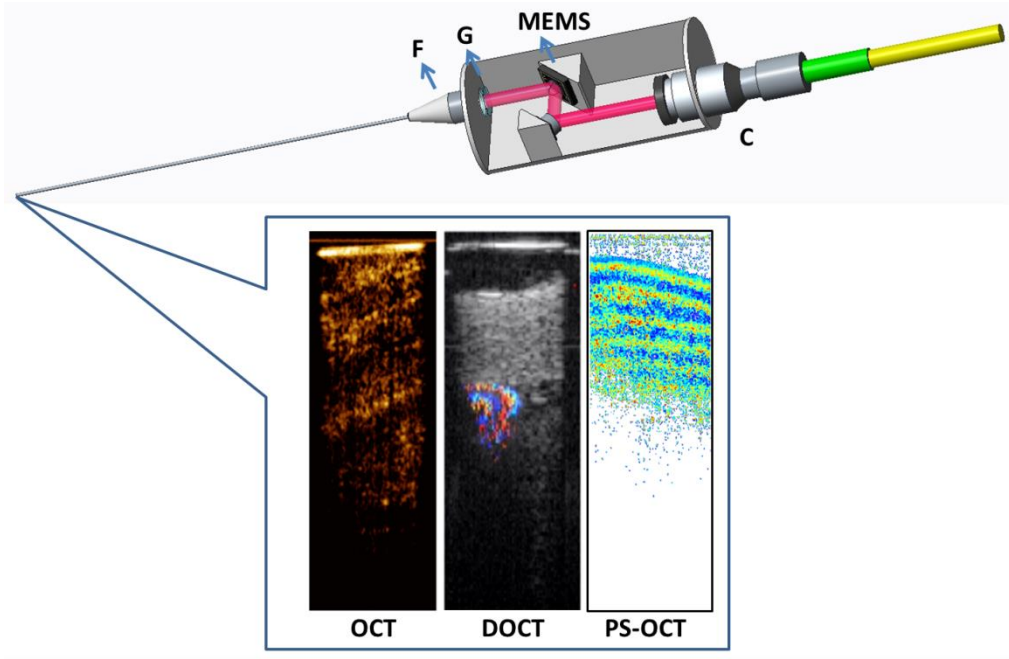

Figure 3. Miniaturized OCT needle probe
F: ferrule, G: GRIN lens, MEMS: microelectromechanical mirrors.

4.2 GRIN lens-based VSDi for brain functional imaging

The research in Chapter 3 aims to use novel optical methods to address the issue that current CCD camera-based imaging system for neuronal functions can only provide two-dimensional information but not offer the functional information beyond the surface. A GRIN lens combined with a microscope has been used in deep brain imaging [19, 122]. In this study, for the first time, we used the GRIN lens in combination with a high-speed CCD camera based VSDi system to study neuronal activities at different depths *in vivo*. There are two aspects we can improve in the near future. One is to combine the GRIN lens-based VSDi system with an OCT system and the other is parallel VSDi imaging of thalamus and cortex using multiple channels.

4.2.1 Needle-type OCT-guided VSDi system

OCT has been reported to reveal depth-resolved dynamics during functional brain activation[61]. However, they used an OCT probe to scan the cortical surface. After combining the OCT system into the same GRIN lens, the needle-type OCT can not only guide the probe to the precise location in deep brain, but also serve as an independent channel to record neuron functions by detecting the tissue scattering changes when being activated. In the proposed system, needle-type OCT will be used to detect neuronal functions in the deep brain for the first time. Fig. 4 shows the system setup, a dichroic mirror will be used to integrate OCT/VSDi and to separate the two modalities. The DM2 will allow the fluorescence excitation and emission photons to penetrate, but reflect long wavelength OCT photons (1310nm). Both OCT sample arm and VSDi excitation photons will be coupled into the same GRIN lens,

but VSDi emission photons and OCT scattering photons will be divided into two different paths based on their wavelengths.

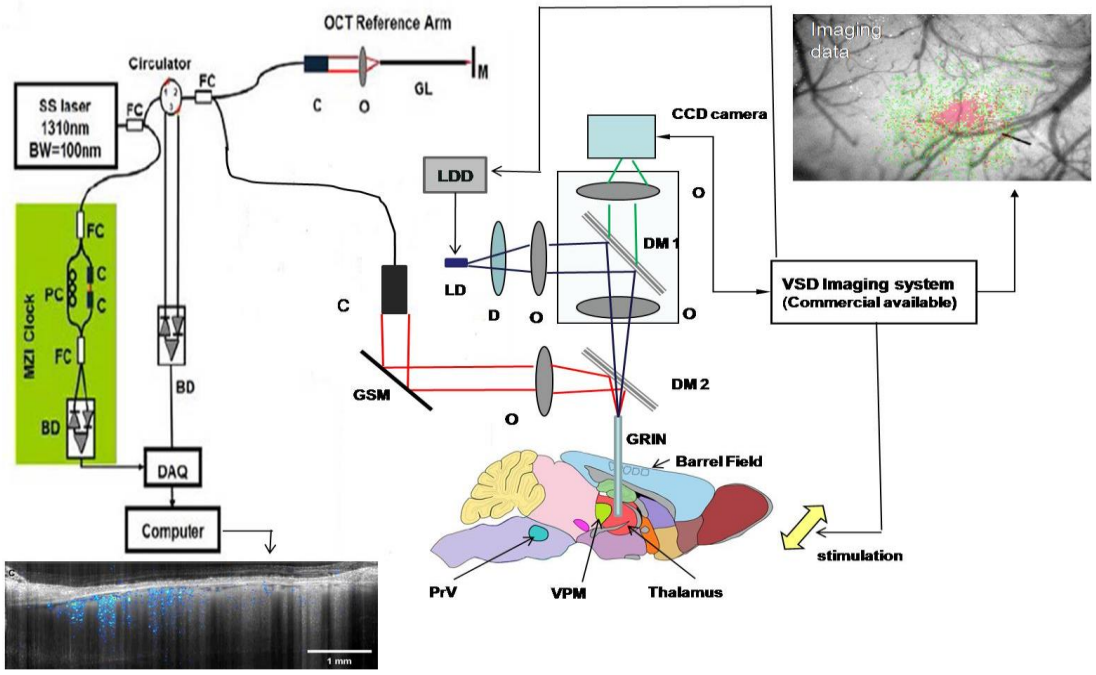

Figure 4. Schematic of the needle-type OCT-guided VSDi system
FC: fiber coupler; PC: polarization controller; C: collimator, BD: balanced detector, MZI: Mach-Zehnder interferometer (frequency clocks), DAQ: data acquisition board, M: mirror, GSM: galvonometer scanning mirror, O: objective lens, D: diffuser, LD: laser diode, LLD: laser diode driver; DM: dichroic mirror; GL: GRIN [58, 61, 123].

In this system, OCT will provide real-time imaging feedback for avoiding at-risk vessels and guiding the instrument to specific targets. Then OCT and VSDi will provide two independent channels to observe neural activities at various regions with different depth during stimulation *in vivo*, whithe ch will definitely serve as a very useful system for neuroscience. . Furthermore, binding properties of VSD to active neurons may provide an enhanced signal for OCT functional imaging.

4.2.2 Multiple channels for parallel VSDi imaging of thalamus and cortex

In order to record neural activities in thalamus and cortex simultaneously, we have built a two-channel VSDi imaging system as shown in Fig. 5. The two-channel

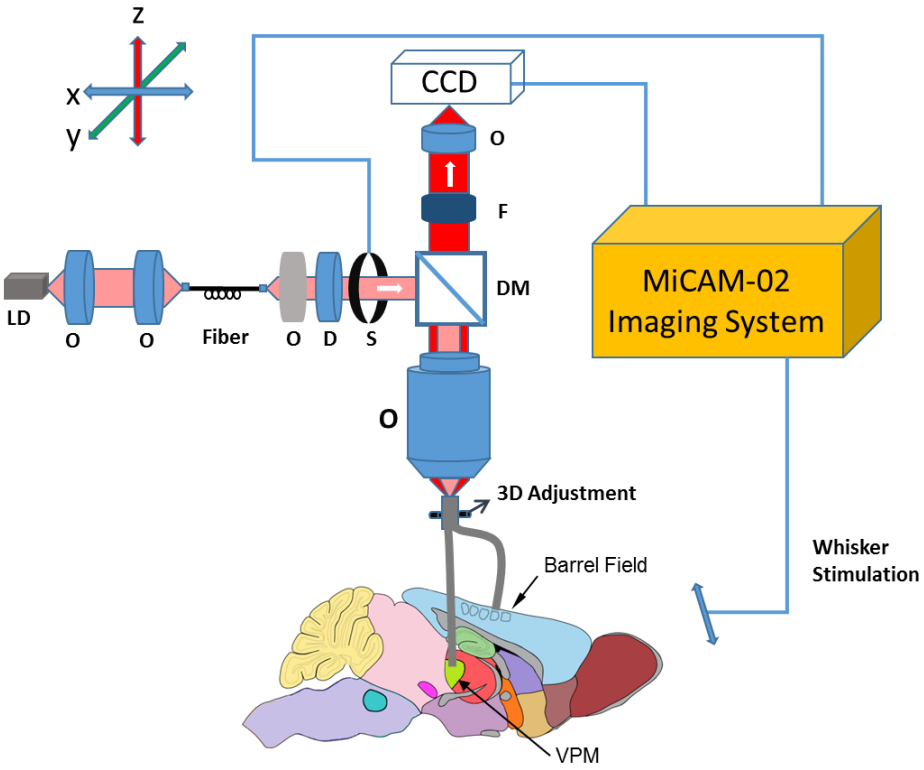

Figure 5. Schematic of the two-channel VSDi needle system
O: objective lens; S: shutter; D: diffuser; F: filter; DM: dichroic mirror; GL: GRIN rod lens.

system consists of one rigid 1-mm GRIN lens and one flexible 1-mm fiber bundle. During the experiment, the rigid GRIN lens was inserted into the brain above the thalamus and the soft fiber bundle was put on the cortex by a 3D manipulator as shown in Fig. 6. Figure 7(a) depicts C2 whisker stimulation. Figure 7(b) shows changes in fluorescence (ΔF/F) in response to C2 whisker stimulation from thalamus and cortex. Clearly the changes in fluorescence (ΔF/F) started earlier than that in the cortex. Figure 7(c) shows the images of changes in fluorescence signals in response to

contralateral C2 whisker stimulation from thalamus and cortex. The signal in thalamus appeared about 25 ms after the stimulus onset, and reached its peak at 50-55 ms after the stimulus onset while the signal in cortex appeared about 30 ms after the stimulus onset, and reached its peak at 45-50 ms after the stimulus onset. After 75 ms, the activated signals disappeared gradually. An interesting observation is that the signal in thalamus appeared earlier and disappeared later, which means the signal lasted longer in thalamus. An interpretation is that the signal appeared in thalamus first. The signal was then transmitted to cortex, and the response in cortex gave some feedback to thalamus. We will use this multiple channel system for parallel VSDi imaging of thalamus and cortex to investigate the corticothalamic loop in the next step.

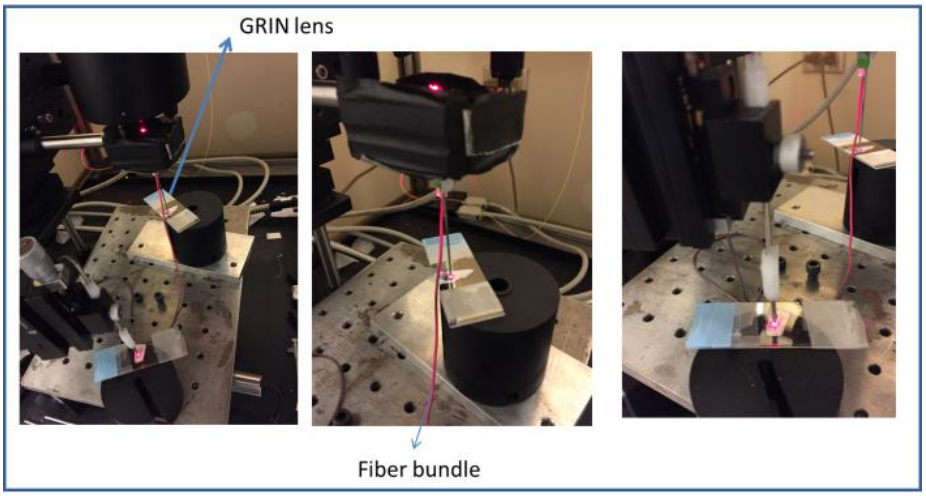

Figure 6. Two-channel VSDi system.

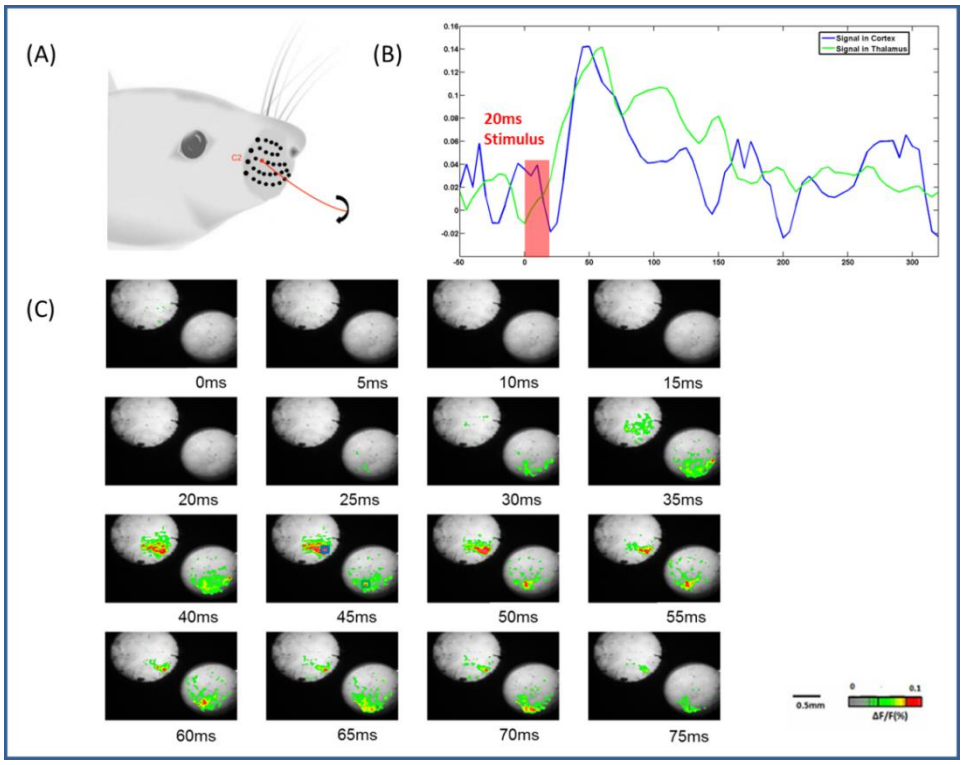

Figure 7. VPM and cortex responses to stimulation of single whisker

(a) C2 whisker for stimulation. (b) Changes in fluorescence (ΔF/F(%), ordinate) in response to C2 whisker stimulation from thalamus and cortex. Fluorescence signal was recorded from the small green and blue square (5 by 5 pixels) marked on the image shown in Figure 6(c) at 45 ms. (c) Voltage-sensitive dye optical images showing single-whisker (C2) stimulation fluorescence changes in the thalamus and cortex. Time period after stimulation is indicated at the bottom left corner of each image.

Developing and validating novel imaging methods will definitely advance in uncovering the neural functions in different levels. The ability to probe neuron activities in the subcortex and deep brain *in vivo* is quite exciting. We believe that these novel systems will yield a high impact on neuroscience and significantly further understanding of the functional maps in the mammalian brain. Furthermore, it will help to reveal the inner mechanisms of neuronal diseases in a more straightforward way, which will undoubtedly provide a convincing manner in neuronal disease detection and treatment evaluation.

Bibliography

1. Heran, M.K., Smith, A.D. & Legiehn, G.M. Spinal injection procedures: a review of concepts, controversies, and complications. *Radiol Clin North Am* **46**, 487-514, v-vi (2008).
2. Scott, D.B. Identification of the epidural space: loss of resistance to air or saline? *Reg Anesth* **22**, 1-2 (1997).
3. Rathmell, J.P. et al. Identification of the epidural space with optical spectroscopy: an in vivo swine study. *Anesthesiology* **113**, 1406-18 (2010).
4. Grau, T., Leipold, R.W., Conradi, R., Martin, E. & Motsch, J. Efficacy of ultrasound imaging in obstetric epidural anesthesia. *Journal of clinical anesthesia* **14**, 169-175 (2002).
5. Jeng, C.L., Torrillo, T.M. & Rosenblatt, M.A. Complications of peripheral nerve blocks. *British Journal Of Anaesthesia* **105**, I97-I107 (2010).
6. Curatolo, M., Orlando, A., Zbinden, A.M., Scaramozzino, P. & Venuti, F.S. A multifactorial analysis to explain inadequate surgical analgesia after extradural block. *Br J Anaesth* **75**, 274-81 (1995).
7. Rigg, J.R. et al. Epidural anaesthesia and analgesia and outcome of major surgery: a randomised trial. *Lancet* **359**, 1276-82 (2002).
8. Ho, K.Y. Vascular uptake of contrast despite negative aspiration in interlaminar cervical epidural injection. *Pain Physician* **9**, 267-8 (2006).
9. Hodges, S.D., Castleberg, R.L., Miller, T., Ward, R. & Thornburg, C. Cervical epidural steroid injection with intrinsic spinal cord damage. Two case reports. *Spine (Phila Pa 1976)* **23**, 2137-42; discussion 2141-2 (1998).
10. Tripathi, M., Nath, S.S. & Gupta, R.K. Paraplegia after intracord injection during attempted epidural steroid injection in an awake-patient. *Anesth Analg* **101**, 1209-11, table of contents (2005).
11. Tang, Q., Liang, C.-P., Wu, K., Sandler, A. & Chen, Y. Real-time epidural anesthesia guidance using optical coherence tomography needle probe. *Quantitative Imaging in Medicine and Surgery* **5**, 118-124 (2014).
12. Muto, A., Ohkura, M., Abe, G., Nakai, J. & Kawakami, K. Real-time visualization of neuronal activity during perception. *Curr Biol* **23**, 307-11.
13. Lenkov, D.N., Volnova, A.B., Pope, A.R. & Tsytsarev, V. Advantages and limitations of brain imaging methods in the research of absence epilepsy in humans and animal models. *J Neurosci Methods* **212**, 195-202.
14. Hillman, E.M. Optical brain imaging in vivo: techniques and applications from animal to man. *J Biomed Opt* **12**, 051402 (2007).
15. Lutcke, H. et al. Optical recording of neuronal activity with a genetically-encoded calcium indicator in anesthetized and freely moving mice. *Front Neural Circuits* **4**, 9.
16. Sato, K. et al. Intraoperative intrinsic optical imaging of neuronal activity from subdivisions of the human primary somatosensory cortex. *Cereb Cortex* **12**, 269-80 (2002).
17. Baker, B.J. et al. Imaging brain activity with voltage- and calcium-sensitive dyes. *Cell Mol Neurobiol* **25**, 245-82 (2005).

18. Aguirre, A.D. et al. Depth-resolved imaging of functional activation in the rat cerebral cortex using optical coherence tomography. *Opt Lett* **31**, 3459-61 (2006).
19. Jung, J.C., Mehta, A.D., Aksay, E., Stepnoski, R. & Schnitzer, M.J. In vivo mammalian brain imaging using one- and two-photon fluorescence microendoscopy. *J Neurophysiol* **92**, 3121-33 (2004).
20. Huang, D. et al. Optical coherence tomography. *Science* **254**, 1178-1181 (1991).
21. Bouma, B.E. & Tearney, G.J. Clinical imaging with optical coherence tomography. *Academic Radiology* **9**, 942-53 (2002).
22. Li, X.D. et al. Optical coherence tomography: Advanced technology for the endoscopic imaging of Barrett's esophagus. *Endoscopy* **32**, 921-930 (2000).
23. Wang, R.K. Optical Microangiography: A Label Free 3D Imaging Technology to Visualize and Quantify Blood Circulations within Tissue Beds in vivo. *IEEE J Sel Top Quantum Electron* **16**, 545-554 (2010).
24. Chen, Z., Milner, T.E., Dave, D. & Nelson, J.S. Optical Doppler tomographic imaging of fluid flow velocity in highly scattering media. *Optics Letters* **22**, 64-6 (1997).
25. Choma, M.A., Sarunic, M.V., Yang, C.H. & Izatt, J.A. Sensitivity advantage of swept source and Fourier domain optical coherence tomography. *Optics Express* **11**, 2183-2189 (2003).
26. de Boer, J.F. et al. Improved signal-to-noise ratio in spectral-domain compared with time-domain optical coherence tomography. *Optics Letters* **28**, 2067-2069 (2003).
27. Leitgeb, R., Hitzenberger, C.K. & Fercher, A.F. Performance of Fourier domain vs. time domain optical coherence tomography. *Optics Express* **11**, 889-894 (2003).
28. Chen, Z.P. et al. Noninvasive imaging of in vivo blood flow velocity using optical Doppler tomography. *Optics Letters* **22**, 1119-1121 (1997).
29. Izatt, J.A., Kulkami, M.D., Yazdanfar, S., Barton, J.K. & Welch, A.J. In vivo bidirectional color Doppler flow imaging of picoliter blood volumes using optical coherence tomograghy. *Optics Letters* **22**, 1439-1441 (1997).
30. Zhao, Y.H. et al. Doppler standard deviation imaging for clinical monitoring of in vivo human skin blood flow. *Optics Letters* **25**, 1358-1360 (2000).
31. Choi, W. et al. Choriocapillaris and choroidal microvasculature imaging with ultrahigh speed OCT angiography. *PLoS One* **8**, e81499 (2013).
32. Drexler, W. et al. Optical coherence tomography today: speed, contrast, and multimodality. *J Biomed Opt* **19**, 071412 (2014).
33. Mariampillai, A. et al. Speckle variance detection of microvasculature using swept-source optical coherence tomography. *Optics Letters* **33**, 1530-1532 (2008).
34. Ding, Z., Liang, C.-P. & Chen, Y. Technology developments and biomedical applications of polarization-sensitive optical coherence tomography. *Frontiers of Optoelectronics*, 1-13 (2015).

35. Al-Qaisi, M.K. & Akkin, T. Swept-source polarization-sensitive optical coherence tomography based on polarization-maintaining fiber. *Opt Express* **18**, 3392-403 (2010).
36. Jiao, S. & Wang, L.V. Two-dimensional depth-resolved Mueller matrix of biological tissue measured with double-beam polarization-sensitive optical coherence tomography. *Opt Lett* **27**, 101-3 (2002).
37. Raphael, D.T. et al. Images of spinal nerves and adjacent structures with optical coherence tomography: preliminary animal studies. *The Journal of Pain* **8**, 767-773 (2007).
38. Li, X., Chudoba, C., Ko, T., Pitris, C. & Fujimoto, J.G. Imaging needle for optical coherence tomography. *Optics Letters* **25**, 1520-2 (2000).
39. Han, S., Sarunic, M.V., Wu, J., Humayun, M. & Yang, C. Handheld forward-imaging needle endoscope for ophthalmic optical coherence tomography inspection. *J Biomed Opt* **13**, 020505 (2008).
40. Liang, C.P. et al. A forward-imaging needle-type OCT probe for image guided stereotactic procedures. *Opt Express* **19**, 26283-26294 (2011).
41. Jung, J.C. & Schnitzer, M.J. Multiphoton endoscopy. *Opt Lett* **28**, 902-4 (2003).
42. Levene, M.J., Dombeck, D.A., Kasischke, K.A., Molloy, R.P. & Webb, W.W. In vivo multiphoton microscopy of deep brain tissue. *J Neurophysiol* **91**, 1908-12 (2004).
43. Messerschmidt, B., Possner, U. & Houde-Walter, S.N. Fabrication tolerances and metrology requirements for ion-exchanged micro-optic lenses: What's good enough? *Appl Opt* **36**, 8145-52 (1997).
44. Reed, W.A., Yan, M.F. & Schnitzer, M.J. Gradient-index fiber-optic microprobes for minimally invasive in vivo low-coherence interferometry. *Opt Lett* **27**, 1794-6 (2002).
45. Rivas-Moscoso, J.M., Gomez-Reino, C. & Perez, M.V. Fresnel zones in tapered gradient-index media. *J Opt Soc Am A Opt Image Sci Vis* **19**, 2253-64 (2002).
46. Feldman, D.E. & Brecht, M. Map plasticity in somatosensory cortex. *Science* **310**, 810-5 (2005).
47. Erzurumlu, R.S., Murakami, Y. & Rijli, F.M. Mapping the face in the somatosensory brainstem. *Nat Rev Neurosci* **11**, 252-63.
48. Tang, Q. et al. In Vivo Voltage-Sensitive Dye Imaging of Subcortical Brain Function. *Sci Rep* **5**, 17325 (2015).
49. Chen-Bee, C.H., Zhou, Y., Jacobs, N.S., Lim, B. & Frostig, R.D. Whisker array functional representation in rat barrel cortex: transcendence of one-to-one topography and its underlying mechanism. *Front Neural Circuits* **6**, 93 (2012).
50. Lustig, B.R., Friedman, R.M., Winberry, J.E., Ebner, F.F. & Roe, A.W. Voltage-sensitive dye imaging reveals shifting spatiotemporal spread of whisker-induced activity in rat barrel cortex. *J Neurophysiol* **109**, 2382-92 (2013).

51. Tsytsarev, V., Pope, D., Pumbo, E., Yablonskii, A. & Hofmann, M. Study of the cortical representation of whisker directional deflection using voltage-sensitive dye optical imaging. *Neuroimage* **53**, 233-238 (2010).
52. Grewe, B.F., Langer, D., Kasper, H., Kampa, B.M. & Helmchen, F. High-speed in vivo calcium imaging reveals neuronal network activity with near-millisecond precision. *Nat Methods* **7**, 399-405 (2010).
53. Liao, L.D. et al. Neurovascular coupling: in vivo optical techniques for functional brain imaging. *Biomed Eng Online* **12**, 38 (2013).
54. Mirabella, G., Battiston, S. & Diamond, M.E. Integration of multiple-whisker inputs in rat somatosensory cortex. *Cereb Cortex* **11**, 164-70 (2001).
55. Obaid, A.L. & Salzberg, B.M. Optical recording of electrical activity in guinea-pig enteric networks using voltage-sensitive dyes. *J Vis Exp* (2009).
56. Grinvald, A. & Hildesheim, R. VSDI: a new era in functional imaging of cortical dynamics. *Nat Rev Neurosci* **5**, 874-85 (2004).
57. Zhang, F., Wang, L.P., Boyden, E.S. & Deisseroth, K. Channelrhodopsin-2 and optical control of excitable cells. *Nat Methods* **3**, 785-92 (2006).
58. Tsytsarev, V., Pope, D., Pumbo, E., Yablonskii, A. & Hofmann, M. Study of the cortical representation of whisker directional deflection using voltage-sensitive dye optical imaging. *Neuroimage* **53**, 233-8.
59. Loew, L.M., Scully, S., Simpson, L. & Waggoner, A.S. Evidence for a charge-shift electrochromic mechanism in a probe of membrane potential. *Nature* **281**, 497-9 (1979).
60. Tasaki, I., Watanabe, A., Sandlin, R. & Carnay, L. Changes in fluorescence, turbidity, and birefringence associated with nerve excitation. *Proc Natl Acad Sci U S A* **61**, 883-8 (1968).
61. Chen, Y. et al. Optical coherence tomography (OCT) reveals depth-resolved dynamics during functional brain activation. *J Neurosci Methods* **178**, 162-73 (2009).
62. Saberski, L.R., Kondamuri, S. & Osinubi, O.Y. Identification of the epidural space: Is loss of resistance to air a safe technique?: A review of the complications related to the use of air. *Regional Anesthesia and Pain Medicine* **22**, 3-15 (1997).
63. Grondin, L.S. et al. Success of spinal and epidural labor analgesia: comparison of loss of resistance technique using air versus saline in combined spinal-epidural labor analgesia technique. *Anesthesiology* **111**, 165-72 (2009).
64. Evron, S. et al. Identification of the epidural space: loss of resistance with air, lidocaine, or the combination of air and lidocaine. *Anesth Analg* **99**, 245-50 (2004).
65. McLeod, A., Roche, A. & Fennelly, M. Case series: Ultrasonography may assist epidural insertion in scoliosis patients. *Canadian Journal of Anesthesia* **52**, 717-720 (2005).
66. Stojanovic, M.P. et al. The role of fluoroscopy in cervical epidural steroid injections: an analysis of contrast dispersal patterns. *Spine (Phila Pa 1976)* **27**, 509-14 (2002).

67. Ting, C.-K. et al. A new technique to assist epidural needle placement: fiberoptic-guided insertion using two wavelengths. *Anesthesiology* **112**, 1128-1135 (2010).
68. Richardson, J. & Groen, G.J. Applied epidural anatomy. *Continuing Education in Anaesthesia, Critical Care & Pain* **5**, 98-100 (2005).
69. Ting, C.K. & Chang, Y. Technique of fiber optics used to localize epidural space in piglets. *Opt Express* **18**, 11138-47 (2010).
70. Gong, C.S. et al. Portable optical epidural needle-a CMOS-based system solution and its circuit design. *PLoS One* **9**, e106055 (2014).
71. Lin, S.P. et al. Discriminant analysis for anaesthetic decision-making: an intelligent recognition system for epidural needle insertion. *Br J Anaesth* **108**, 302-7 (2012).
72. Desjardins, A.E. et al. Epidural needle with embedded optical fibers for spectroscopic differentiation of tissue: ex vivo feasibility study. *Biomed Opt Express* **2**, 1452-61 (2011).
73. Xie, T., Guo, S., Chen, Z., Mukai, D. & Brenner, M. GRIN lens rod based probe for endoscopic spectral domain optical coherence tomography with fast dynamic focus tracking. *Opt Express* **14**, 3238-46 (2006).
74. Tsytsarev, V. et al. In vivo imaging of brain metabolism activity using a phosphorescent oxygen-sensitive probe. *J Neurosci Methods* **216**, 146-51 (2013).
75. Tsytsarev, V., Bernardelli, C. & Maslov, K.I. Living Brain Optical Imaging: Technology, Methods and Applications. *J Neurosci Neuroeng* **1**, 180-192 (2012).
76. Li, B., Zhou, F.Y., Luo, Q.M. & Li, P.C. Altered resting-state functional connectivity after cortical spreading depression in mice. *Neuroimage* **63**, 1171-1177 (2012).
77. Dunn, A.K. et al. Simultaneous imaging of total cerebral hemoglobin concentration, oxygenation, and blood flow during functional activation. *Opt Lett* **28**, 28-30 (2003).
78. Tian, F., Alexandrakis, G. & Liu, H. Optimization of probe geometry for diffuse optical brain imaging based on measurement density and distribution. *Appl Opt* **48**, 2496-504 (2009).
79. White, B.R. & Culver, J.P. Phase-encoded retinotopy as an evaluation of diffuse optical neuroimaging. *Neuroimage* **49**, 568-77 (2010).
80. Zhou, C. et al. Diffuse optical monitoring of cerebral hemodynamics in piglet with traumatic brain injury. *J Cereb Blood Flow Metab* **29**, S33-S34 (2009).
81. Srinivasan, V.J., Radhakrishnan, H., Jiang, J.Y., Barry, S. & Cable, A.E. Optical coherence microscopy for deep tissue imaging of the cerebral cortex with intrinsic contrast. *Opt Express* **20**, 2220-39 (2012).
82. Qin, J., Shi, L., Dziennis, S., Reif, R. & Wang, R.K. Fast synchronized dual-wavelength laser speckle imaging system for monitoring hemodynamic changes in a stroke mouse model. *Opt Lett* **37**, 4005-7 (2012).
83. Wang, H. et al. Reconstructing micrometer-scale fiber pathways in the brain: multi-contrast optical coherence tomography based tractography. *Neuroimage* **58**, 984-92 (2011).

84. Yu, L., Nguyen, E., Liu, G., Choi, B. & Chen, Z. Spectral Doppler optical coherence tomography imaging of localized ischemic stroke in a mouse model. *J Biomed Opt* **15**, 066006 (2010).
85. Wang, X. et al. Noninvasive laser-induced photoacoustic tomography for structural and functional in vivo imaging of the brain. *Nat Biotechnol* **21**, 803-6 (2003).
86. McCaslin, A.F., Chen, B.R., Radosevich, A.J., Cauli, B. & Hillman, E.M. In vivo 3D morphology of astrocyte-vasculature interactions in the somatosensory cortex: implications for neurovascular coupling. *J Cereb Blood Flow Metab* **31**, 795-806 (2011).
87. Sakadzic, S. et al. Two-photon high-resolution measurement of partial pressure of oxygen in cerebral vasculature and tissue. *Nat Methods* **7**, 755-9 (2010).
88. Derdikman, D., Hildesheim, R., Ahissar, E., Arieli, A. & Grinvald, A. Imaging spatiotemporal dynamics of surround inhibition in the barrels somatosensory cortex. *J Neurosci* **23**, 3100-5 (2003).
89. Orbach, H.S., Cohen, L.B. & Grinvald, A. Optical mapping of electrical activity in rat somatosensory and visual cortex. *J Neurosci* **5**, 1886-95 (1985).
90. Orbach, H.S. & Cohen, L.B. Optical monitoring of activity from many areas of the in vitro and in vivo salamander olfactory bulb: a new method for studying functional organization in the vertebrate central nervous system. *J Neurosci* **3**, 2251-62 (1983).
91. Kleinfeld, D. & Delaney, K.R. Distributed representation of vibrissa movement in the upper layers of somatosensory cortex revealed with voltage-sensitive dyes. *J Comp Neurol* **375**, 89-108 (1996).
92. Vitali, I. & Jabaudon, D. Synaptic biology of barrel cortex circuit assembly. *Semin Cell Dev Biol* **35**, 156-64 (2014).
93. Erzurumlu, R.S. & Gaspar, P. Development and critical period plasticity of the barrel cortex. *Eur J Neurosci* **35**, 1540-53 (2012).
94. Kim, J.K., Choi, J.W. & Yun, S.H. 350-mum side-view optical probe for imaging the murine brain in vivo from the cortex to the hypothalamus. *J Biomed Opt* **18**, 50502 (2013).
95. Paxinos, G. & Franklin, K. Paxinos and Franklin's the Mouse Brain in Stereotaxic Coordinates (Academic Press, Incorporated, 2012).
96. Lo, F.S., Akkentli, F., Tsytsarev, V. & Erzurumlu, R.S. Functional significance of cortical NMDA receptors in somatosensory information processing. *J Neurophysiol* **110**, 2627-36 (2013).
97. Peters, A.J., Chen, S.X. & Komiyama, T. Emergence of reproducible spatiotemporal activity during motor learning. *Nature* **510**, 263-7 (2014).
98. Tsytsarev, V. et al. In vivo imaging of epileptic activity using 2-NBDG, a fluorescent deoxyglucose analog. *J Neurosci Methods* **203**, 136-40 (2012).
99. Wallace, D.J. & Sakmann, B. Plasticity of representational maps in somatosensory cortex observed by in vivo voltage-sensitive dye imaging. *Cereb Cortex* **18**, 1361-73 (2008).

100. Vnek, N., Ramsden, B.M., Hung, C.P., Goldman-Rakic, P.S. & Roe, A.W. Optical imaging of functional domains in the cortex of the awake and behaving monkey. *Proc Natl Acad Sci U S A* **96**, 4057-60 (1999).
101. Zhou, D., Rangan, A.V., McLaughlin, D.W. & Cai, D. Spatiotemporal dynamics of neuronal population response in the primary visual cortex. *Proc Natl Acad Sci U S A* **110**, 9517-22 (2013).
102. Barnett, M.W. et al. Synaptic Ras GTPase activating protein regulates pattern formation in the trigeminal system of mice. *J Neurosci* **26**, 1355-65 (2006).
103. Alitto, H.J. & Usrey, W.M. Corticothalamic feedback and sensory processing. *Curr Opin Neurobiol* **13**, 440-5 (2003).
104. Kobat, D., Horton, N.G. & Xu, C. In vivo two-photon microscopy to 1.6-mm depth in mouse cortex. *J Biomed Opt* **16**, 106014 (2011).
105. Wang, Z., Li, P., Luo, W., Chen, S. & Luo, Q. Peri-infarct temporal changes in intrinsic optical signal during spreading depression in focal ischemic rat cortex. *Neurosci Lett* **424**, 133-8 (2007).
106. Obaid, A.L. & Salzberg, B.M. Optical recording of electrical activity in guinea-pig enteric networks using voltage-sensitive dyes. *J Vis Exp*, e1631 (2009).
107. Civillico, E.F. & Contreras, D. Integration of evoked responses in supragranular cortex studied with optical recordings in vivo. *J Neurophysiol* **96**, 336-51 (2006).
108. Luo, Z., Volkow, N.D., Heintz, N., Pan, Y. & Du, C. Acute cocaine induces fast activation of D1 receptor and progressive deactivation of D2 receptor striatal neurons: in vivo optical microprobe [Ca2+]i imaging. *J Neurosci* **31**, 13180-90 (2011).
109. Engelbrecht, C.J., Johnston, R.S., Seibel, E.J. & Helmchen, F. Ultra-compact fiber-optic two-photon microscope for functional fluorescence imaging in vivo. *Opt Express* **16**, 5556-64 (2008).
110. Kim, J.K. et al. Fabrication and operation of GRIN probes for in vivo fluorescence cellular imaging of internal organs in small animals. *Nature Protocols* **7**, 1456-1469 (2012).
111. Liang, C.P. et al. A forward-imaging needle-type OCT probe for image guided stereotactic procedures. *Opt Express* **19**, 26283-94 (2011).
112. Narboux-Neme, N. et al. Neurotransmitter Release at the Thalamocortical Synapse Instructs Barrel Formation But Not Axon Patterning in the Somatosensory Cortex. *J Neurosci* **32**, 6183-6196 (2012).
113. Ferezou, I. et al. Spatiotemporal dynamics of cortical sensorimotor integration in behaving mice. *Neuron* **56**, 907-23 (2007).
114. Ferezou, I., Bolea, S. & Petersen, C.C. Visualizing the cortical representation of whisker touch: voltage-sensitive dye imaging in freely moving mice. *Neuron* **50**, 617-29 (2006).
115. Arakawa, H. et al. Thalamic NMDA Receptor Function Is Necessary for Patterning of the Thalamocortical Somatosensory Map and for Sensorimotor Behaviors. *J Neurosci* **34**, 12001-14 (2014).
116. Paukert, M. et al. Norepinephrine controls astroglial responsiveness to local circuit activity. *Neuron* **82**, 1263-70 (2014).

117. Kim, G. & Menon, R. An ultra-small three dimensional computational microscope. *Appl Phys Lett* **105**, 061114 (2014).
118. Hee, M.R., Huang, D., Swanson, E.A. & Fujimoto, J.G. Polarization-sensitive low-coherence reflectometer for birefringence characterization and ranging. *JOSA B* **9**, 903-908 (1992).
119. Al-Qaisi, M.K. & Akkin, T. Swept-source polarization-sensitive optical coherence tomography based on polarization-maintaining fiber. *Optics express* **18**, 3392-3403 (2010).
120. Yamanari, M., Makita, S. & Yasuno, Y. Polarization-sensitive swept-source optical coherence tomography with continuous source polarization modulation. *Optics express* **16**, 5892-5906 (2008).
121. Ding, Z. et al. Imaging Spinal Structures With Polarization-Sensitive Optical Coherence Tomography. *IEEE Photonics Journal* **8**, 1-8 (2016).
122. Luo, Z., Volkow, N.D., Heintz, N., Pan, Y. & Du, C. Acute cocaine induces fast activation of D1 receptor and progressive deactivation of D2 receptor striatal neurons: in vivo optical microprobe [Ca2+]i imaging. *J Neurosci* **31**, 13180-90.
123. Liang, C.P., Huang, T.J., Rao, P.Z. & Chung, S.J. Low-power VCO with phase-noise improvement in 0.18 mu m CMOS technology. *Electronics Letters* **46**, 1385-1387 (2010).